AIAA Science and Technology Forum and Exposition, 6-10 January 2020, Orlando, Florida

A Numerical Investigation of Parachute Deployment in Supersonic Flow

Jonathan Boustani[1,2]*, Gokul Anugrah[1]†,
Michael F. Barad[2]‡, Cetin C. Kiris[2]§, and Christoph Brehm[1]¶

[1] *Department of Mechanical Engineering, University of Kentucky, Lexington, KY 40506, USA.*

[2] *Computational Aerosciences Branch, NASA Ames Research Center, Moffett Field, CA 94035, USA.*

A validated computational fluid-structure interaction method applied to supersonic parachute inflation is extended to consider a unique, parallel self-contact algorithm, porosity interface conditions on the canopy, improved flow field sampling procedures for obtaining quality loading on the parachute canopy, adaptive mesh refinement, and improved treatment of thin geometries in an immersed boundary framework. These extensions are discussed in detail and demonstrated individually on test problems. Finally, the developments are brought together for demonstration on a sub-scale MSL parachute geometry.

I. Motivation and Introduction

Interest in parachute deployment and performance in supersonic flows began in the 1960's and 1970's, spurned by the interests of The U.S. Air Force[1,2] and NASA[3,4] at the time. The parachute geometries considered at the time included modified ringsails, cross parachutes, and disk-gap-band (DGB) parachutes,[5] the latter of which would be used in every mission to the Martian surface due to its stability at relevant Mach number flows in low-density environments.[6] The research conducted during this era resulted in the Viking DGB parachute system and the benchmarks and design criteria that would be the basis of the aforementioned Mars entry missions — until the Mars Science Laboratory (MSL).[7,8]

The MSL Entry, Descent, and Landing (EDL) system sought to utilize the largest nominal diameter parachute used in a Martin landing mission in conjunction with landing the heaviest payload previously considered at the highest altitude landing ever.[9] These demanding objectives required the EDL qualification to expand those design benchmarks set during the Viking era. This resulted in a series of real-world drop tests, wind tunnel tests,[8,10] and well as supporting computational fluid dynamics (CFD)[11] and fluid-structure interaction (FSI)[12] simulations. This large-scale effort resulted in a successful landing of a rover on the Martian surface, but it also highlights the dependence of parachute and EDL system qualification on costly and time consuming real-world experiments.

In addition to this, to investigate EDL systems that could increase the maximum payload weight deliverable to the Martian surface, JPL and NASA started the low-density supersonic decelerator (LDSD) project.[13] In these missions, inflatable decelerators followed by modified ringsail parachutes, which were argued to provide better drag performance than DGB parachutes, were used in two test flights (in 2014 and 2015) to decelerate a payload returning to the terrestrial atmosphere. In both test flights, there were issues with the employed parachute system. In the first test, the parachute failed to open, and in the second test, the canopy suffered tears. The inflatable decelerators seemed to work, but the tests were only partially successful because of the performance of the parachute systems.[14] This highlights some of the uncertainty that still exists when extrapolating design criteria from established missions to consider new, larger parachute

---

*NASA Pathways Student, Ph.D. Candidate, AIAA member.

†Ph.D. Student, AIAA member.

‡Senior Research Scientist, AIAA member.

§Branch Chief, Senior AIAA member.

¶Assistant Professor, AIAA member.

designs as well as short-comings in the ability to predict inflation times and the presence of asymmetric loading and its effect on the integrity of the canopy.[14]

Most recently, starting in 2017, the Advanced Supersonic Parachute Inflation Research Experiments (ASPIRE) sought to mitigate risk for the Mars 2020 mission by testing and developing capabilities to experiment with candidate parachutes at supersonic conditions relevant to inflation in the upper Martian atmosphere.[15] The project oversaw three successful parachutes inflating during experiments conducted in the upper terrestrial atmosphere, one of which is shown in Fig. 1. Though these tests were successful, and new, strengthened parachute designs were considered, CFD simulations played only a supporting role.[16]

The increasingly demanding landing objectives will require EDL systems and supersonic parachutes to become qualified again through a series of real-world drop tests and wind tunnel tests, especially as parachute designs that have not been tested in the Martian atmosphere are considered.[13, 14] Hence, the main motivation for this research is to increase NASA's simulation prediction capabilities of supersonic parachute deployment and flight performance to investigate new designs and potential paths to failure during the inflation process through the development of high-fidelity and efficient numerical methods.

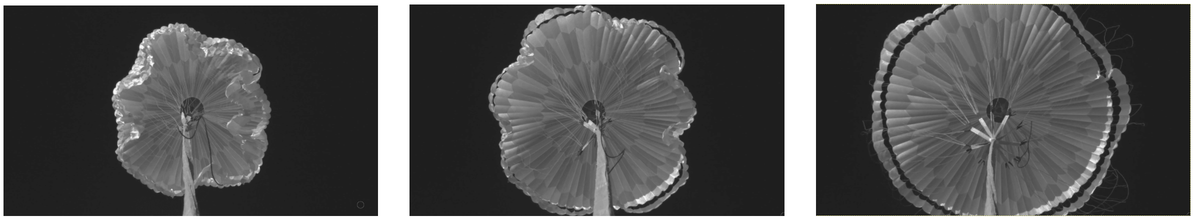

Figure 1: Snapshots in time of canopy inflation in the upper terrestrial atmosphere from the ASPIRE SR03 test using a parachute similar to that used by MSL. Images adjusted from Ref. 17.

Some research has been conducted with similar goals through the use of coupling CFD and computational structural dynamics (CSD) codes for simulating the nonlinear FSI phenomena present during supersonic parachute flight. Some of the first true FSI simulations of supersonic parachute flight may have been conducted in 2005 by Vorticity Ltd in Ref. 18 followed in 2007 by Ref. 19. In these works, LS-DYNA was used to simulate the inflated dynamics of the Huygens[18] and MSL[19] EDL systems. The simulations were able to capture the partial collapse and re-inflation of a DGB parachute canopy and provide insight on the effect of the trailing distance of the canopy behind the wake of the capsule — it was found that if the canopy was too close, it was more likely to collapse.

Following this, large period, drastic area oscillations in sustained parachute flight have been studied by Karagiozis *et al.*[12] using the Favre-filtered Navier-Stokes equations within a Cartesian adaptive mesh refinement framework. This work was recently extended to solving the Favre-filtered compressible Navier-Stokes equations using a PI-controller based IBM.[20] Both works found the presence of area oscillations and its behavior to depend dramatically on the grid resolution. Another aspect of supersonic parachute performance, notably, the inflation, has been studied by a joint research initiative between the Farhat Research Group at Stanford University and NASA's Jet Propulsion Laboratory.[21] This work is based on solving the compressible Navier-Stokes equations using an unstructured, embedded boundary method with adaptive mesh refinement[22] and has considered the effect of the initial folding state and stress state of the parachute on the drag history and performance of a parachute in supersonic flow. This work also considers orthotropic and materially nonlinear constitutive relations and porosity models for the parachute canopy.

The method used in this paper is the continuation of past research efforts involving the development of fluid-structure interaction (FSI) simulation capabilities by coupling geometrically linear[23] and geometrically nonlinear[24] structural finite element solvers with a higher-order IBM for the compressible Navier-Stokes equations[25–27] applied to canonical[24] and realistic[28] large deformation FSI test cases in a variety of flow regimes. The objective of the current paper is to improve the fidelity of simulations involving supersonic parachute deployment[28] by including newly-developed, fully-parallel self-contact identification and forcing methods, porosity boundary conditions on the parachute canopy, improved, robust flow field sampling procedures to obtain quality loading on the parachute canopy, adaptive mesh refinement, and improved treatment of very thin geometries in an IBM framework. These improvements to the fidelity of parachute inflation simulations aid the goal of improving NASA's simulation prediction capabilities of complex, nonlinear fluid-structure interactions relevant to parachute performance in supersonic conditions.

The current paper will proceed as follows: first, Sec. II describes the governing equations of both the fluid and structural solvers followed by their discretization and numerical implementation in Sec. III and the improvements made therein. Next, Sec. IV contains a brief overview of the loosely coupled, fully-parallel FSI coupling approach used in this research. Finally, Sec. V details simulations of the inflation of a sub-scale MSL parachute geometry in conditions resembling the upper Martian atmosphere as a test bed for demonstrating the aforementioned developments.

II. Governing Equations

The computational method is composed of a geometrically nonlinear structural finite element solver coupled with a higher-order IBM fluid dynamics solver. The computational structural dynamics (CSD) solver considers the incremental Total Lagrangian equations of motion, and the computational fluid dynamics solver (CFD) considers the compressible Navier-Stokes equations. The governing equations for each domain are summarized in this section as well as the equations governing the interaction between the fluid and the structure. The numerical methods to solve these equations are described in the following Section III.

A. Compressible Navier-Stokes Equations

The CFD solver considers the flow of an ideal, non-reactive gas described by the compressible Navier-Stokes equations, shown here in conservative form:

$$\frac{\partial \mathbf{W}}{\partial t} + \frac{\partial \mathbf{E}}{\partial x} + \frac{\partial \mathbf{F}}{\partial y} + \frac{\partial \mathbf{G}}{\partial z} = 0, \tag{1}$$

where $\mathbf{W}$ is the conservative variable vector

$$\mathbf{W} = \left[\; \rho, \rho u, \rho v, \rho w, \rho e_t \; \right]^T,$$

and $\mathbf{E}$, $\mathbf{F}$, and $\mathbf{G}$ are the total flux vectors given by

$$\mathbf{E} = \begin{bmatrix} \rho u \\ \rho u^2 + p - \mu\tau_{xx} \\ \rho uv - \mu\tau_{xy} \\ \rho uw - \mu\tau_{xz} \\ (\rho e_T + p)u - \mu u\tau_{xx} - \mu v\tau_{xy} - \mu w\tau_{xz} + q_x \end{bmatrix}, \mathbf{F} = \begin{bmatrix} \rho v \\ \rho uv - \mu\tau_{xy} \\ \rho v^2 + p - \mu\tau_{yy} \\ \rho uw - \mu\tau_{yz} \\ (\rho e_T + p)v - \mu u\tau_{xy} - \mu v\tau_{yy} - \mu w\tau_{yz} + q_y \end{bmatrix}, \text{ and}$$

$$\mathbf{G} = \begin{bmatrix} \rho w \\ \rho uw - \mu\tau_{xz} \\ \rho vw - \mu\tau_{yz} \\ \rho w^2 + p - \mu\tau_{zz} \\ (\rho e_T + p)w - \mu u\tau_{xz} - \mu v\tau_{yz} - \mu w\tau_{zz} + q_z \end{bmatrix}.$$

In the given expressions for the conservative form of the compressible Navier-Stokes equations, ρ represents the density of the fluid, u, v, w represent the three velocity components, p represents the pressure, and e_T represents the total energy, given by

$$e_T = e + \frac{u^2 + v^2 + w^2}{2}. \tag{2}$$

The components of the symmetric shear-stress tensor can be evaluated as

$$\tau_{xx} = \frac{2}{3}\left(2\frac{\partial u}{\partial x} - \frac{\partial v}{\partial y} - \frac{\partial w}{\partial z}\right), \tau_{yy} = \frac{2}{3}\left(2\frac{\partial v}{\partial y} - \frac{\partial u}{\partial x} - \frac{\partial w}{\partial z}\right), \tau_{zz} = \frac{2}{3}\left(2\frac{\partial w}{\partial z} - \frac{\partial u}{\partial x} - \frac{\partial v}{\partial y}\right), \tag{3}$$

$$\tau_{xy} = \left(\frac{\partial u}{\partial y} + \frac{\partial v}{\partial x}\right), \tau_{xz} = \left(\frac{\partial u}{\partial z} + \frac{\partial w}{\partial x}\right), \text{ and} \tau_{yz} = \left(\frac{\partial v}{\partial z} + \frac{\partial w}{\partial y}\right).$$

The components of the heat-flux are given as

$$q_x = -k\frac{\partial T}{\partial x}, \quad q_y = -k\frac{\partial T}{\partial y}, \quad \text{and} \quad q_z = -k\frac{\partial T}{\partial z}. \tag{4}$$

where T represents the temperature of the fluid and k represents the thermal conductivity of the fluid.

B. Total Lagrangian Incremental Equation of Motion

The finite element formulation used in the proposed research to perform the computational structural dynamics simulations is derived from the continuum mechanics formulation of the incremental equations of motion. One of the core principles of this formulation is 'The Principle of Virtual Work'. This can be expressed as

$$\int_V \overline{\boldsymbol{\epsilon}}^T \boldsymbol{\tau} \, dV = \int_V \overline{\boldsymbol{U}}^T \boldsymbol{f}^B \, dV + \int_{s_f} \overline{\boldsymbol{U}}^{s_f\,T} \boldsymbol{f}^{s_f} \, dS + \sum_i \overline{\boldsymbol{U}}^{iT} \boldsymbol{R}_C^i, \tag{5}$$

where $\overline{\boldsymbol{\epsilon}}$ represents the virtual strains corresponding to virtual displacements $\overline{\boldsymbol{U}}$, $\boldsymbol{\tau}$ represents the internal stresses generated due to the virtual strains, and the right-hand side terms from left to right represent the external loading due to body forces, surface forces, and point loads, respectively.

Expressing the strain and stress terms in the Principle of Virtual Work with those corresponding to the Total Lagrangian Formulation, the Green-Lagrange strain tensor and the Second Piola-Kirchoff stress tensor, given by

$${}^t_0\boldsymbol{\epsilon}_{ij} = \frac{1}{2}({}^t_0\boldsymbol{u}_{i,j} + {}^t_0\boldsymbol{u}_{j,i} + {}^t_0\boldsymbol{u}_{k,i}\,{}^t_0\boldsymbol{u}_{k,j}) \text{ and } {}^t_0\boldsymbol{S}_{ij} = {}^t_0\boldsymbol{C}_{ijrs}\,{}^t_0\boldsymbol{\epsilon}_{rs}, \tag{6}$$

respectively, the Total Lagrangian incremental equation of motion can be obtained about an equilibrium configuration in the reference state.

The final equation of motion is then given as

$$\int_{{}^0V} {}_0\boldsymbol{S}_{ij}\delta_0\boldsymbol{\epsilon}_{ij} d^0V + \int_{{}^0V} {}^t_0\boldsymbol{S}_{ij}\delta_0\boldsymbol{\eta}_{ij} d^0V = {}^{t+\Delta t}\boldsymbol{\mathcal{R}} - \int_{{}^0V} {}^t_0\boldsymbol{S}_{ij}\delta_0\boldsymbol{e}_{ij} d^0V, \tag{7}$$

where the left-most term on the left-hand-side represents the contribution from the linear portion of the Green-Lagrange strain, $\delta_0\boldsymbol{\epsilon}_{ij}$, and the right-most term on the left-hand-side represents the contribution from the nonlinear portion, $\delta_0\boldsymbol{\eta}_{ij}$. The right-hand-side represents the balance of external, ${}^{t+\Delta t}\boldsymbol{\mathcal{R}}$, and internal work.

C. Coupling Boundary Conditions

The fluid and structure interact through the transfer of loads on the shared boundary and the displacement and velocity of the shared boundary. Specifically, the fluid domain provides the traction $\mathbf{t}(\overline{\mathbf{x}}_b(t), t)$ for the structure such that

$$\mathbf{t}_{structure}(\overline{\mathbf{x}}_b(t), t) = \mathbf{t}_{fluid}(\overline{\mathbf{x}}_b(t), t), \tag{8}$$

at the shared boundary $\overline{\mathbf{x}}_b(t)$, and the structural domain provides the position and velocity of the shared boundary $\overline{\mathbf{x}}_b(t)$ such that

$$\overline{\mathbf{x}}_b(t) = \mathbf{x}_{fluid}(t) = \mathbf{x}_{structure}(t), \text{ and} \tag{9}$$

$$\dot{\overline{\mathbf{x}}}_b(t) = \dot{\mathbf{x}}_{fluid}(t) = \dot{\mathbf{x}}_{structure}(t) \;\; \forall t \geq 0. \tag{10}$$

III. Computational Method

The computational methods that are be used to solve the governing equations are presented in this section. Extended details of the CFD solver and the IBM it employs are presented and validated in many prior works,[25–27, 29, 30] and details and validation of the structural solver can be found in Boustani *et al.*[24] and Boustani *et al.*[28] As such, a short overview of each solver is presented here with the focus on the detailed descriptions of new improvements towards increasing the overall robustness and fidelity of the method. The details on the computational methods used to enforce the coupling conditions are presented in Sec. IV, along with a summary of the FSI algorithm.

A. Immersed Boundary Method

IBMs are advantageous for moving boundary problems because of the automatic volume mesh generation for arbitrarily complex geometries. This is demonstrated in Fig.2a with a complex parachute geometry immersed in a Cartesian framework. As has been stated and introduced in prior works, an established higher-order, structured Cartesian, sharp IBM introduced in Brehm and Fasel[29] is utilized to solve the compressible Navier-Stokes equations, usually with the 2nd- or 4th-order Runge-Kutta explicit time integration scheme and the 5th-order Weighted Essentially Non-oscillatory (WENO) scheme for the convective terms. In this work, the viscous terms are treated with second-order centered finite-difference operators.

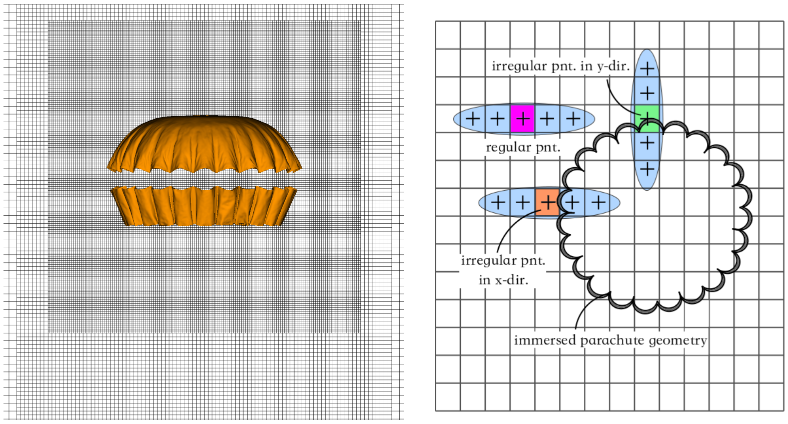

(a) (b)

Figure 2: (a) Demonstration of a complex geometry ‘immersed’ in a Cartesian mesh utilizing the employed IBM’s automatic volume mesh generation and (b) illustration of regular and irregular points and their WENO5 stencils in the vicinity of a 2D parachute geometry immersed in a Cartesian framework.

The key aspects of the employed IBM are that (1) stability is built into the derivation of the method *a priori* rather than proved via demonstration later and (2) the finite difference stencil coefficients for irregular points are locally optimized considering the local flow conditions and distance to the wall to obtain an overall stable discretization. In this work, an irregular grid point is defined as a point where the regular finite difference stencil would reach into or across the representation of the geometry (see Fig. 2b). In practice, these points are identified via an x-ray tracing algorithm[25] as illustrated in Fig. 3a. The recent developments in the IBM take advantage of the x-ray tracing process and the identification of the Cartesian grid pierce points for flow field sampling, self-contact, and the porous media interface condition, as will be described in the coming sections. More details of the derivation of the method, applications, and implementation into NASA’s Launch Ascent and Vehicle Aerodynamics framework can be found in Refs. 25–27, 31–33. Applications of the employed IBM and details pertaining to FSI simulations can be found in Refs. 23, 24, and 28.

The recent developments made to the IBM that are intended to increase the robustness and fidelity when considering thin parachute geometries include: (1) robust flow field sampling for quality loading on the parachute despite the narrow folds and sharp edges that can occur, (2) parallel self-contact identification and enforcement to prevent the parachute from intersecting itself while undergoing massive deformations, (3) porous media boundary conditions to simulate the permeability of parachute broadcloth, and (4) adaptive mesh refinement (AMR) to efficiently track the parachute as it undergoes massive deformations and track the canopy bow shock and wake. These developments will be discussed in detail in the following four sub-sections.

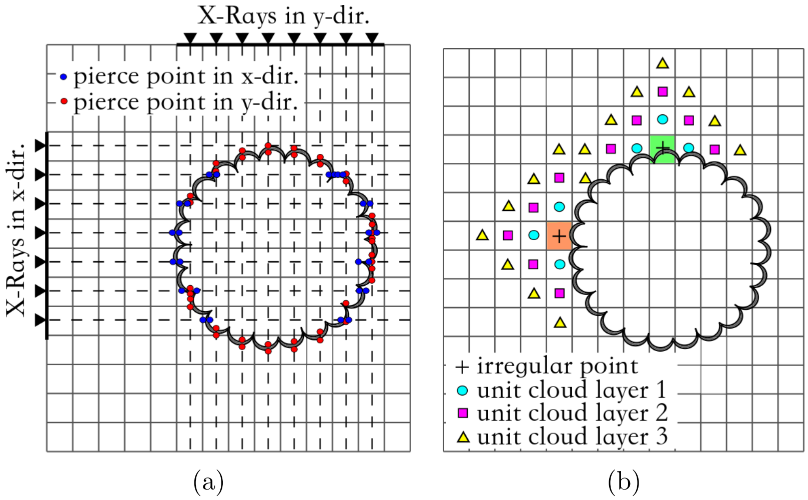

Figure 3: (a) Illustration of the x-ray tracing process and pierce point identification on a complex geometry and (b) illustration of the full cloud creation via graph walking adding successive unit cloud layers.

1. *Robust Flow Field Sampling*

During simulations of parachute inflation, the geometry undergoes massive topological changes as it is displaced by the structural response to the fluid forces. Despite experiencing very complex topologies, the CFD solver must be able to provide quality forces to the CSD solver via extrapolation from the surrounding flow field. This process is conducted by elements on the geometry representation determining a cloud of fluid points in the vicinity of the element, computing interpolation coefficients based on weight-least-squares (WLSQR) techniques, and using the coefficients and interpolation clouds to obtain the flow field quantities on the element face. While in theory this procedure seems routine, experience has shown that the computation of 'good' interpolation point clouds can be challenging when dealing with very thin geometries undergoing massive deformations that fold over or contact itself over regions of flow.

To alleviate this problem and to create a robust sampling method, a mapping was created between the irregular grid points in the fluid domain (described earlier) and the elements on the geometry representation. The reason for this is that the irregular points carefully build full point clouds using 'unit' clouds. In other words, an irregular point adds the points immediately around it into the full cloud if the points (1) are not inside the geometry or, for very thin geometries, (2) do not have 2 pierce points between it and the irregular point in question. These points then do the same procedure until a desired number of interpolation points are added to the full point cloud. This process is illustrated in Fig. 3b. The distinction between criteria (1) and (2) is an important distinction to make when considering extremely thin geometries (such as a parachute) where it is impractical to maintain fluid points inside the entire geometry, but an irregular point should not use an interpolation cloud that reaches across a thin geometry. The use of pierce points in the graph walking approach to create full point clouds accounts for the short-comings in an Eulerian distance function-based approach where the identification of points inside/outside the geometry is straight forward, but the identification of which 'side' of the geometry a point is on is not clear.

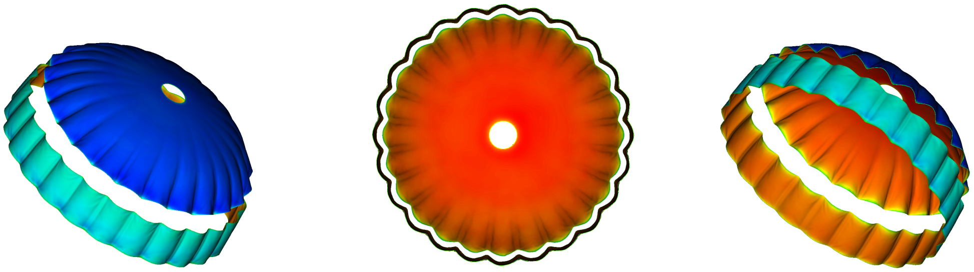

Figure 4: Perspective views of the pressure distribution sampled onto the geometry representation from a surrounding supersonic flow field during an FSI parachute simulation.

This careful process yields interpolation clouds that grow inside narrow folds and along the surface of very complex geometries, and because of their vicinity to the wall, these clouds are ideal candidates for flow field sampling. The full flow field sampling algorithm that is conducted every timestep in moving boundary problems and once for cases with a static geometry is listed in Alg. 1, and it is also demonstrated with a snapshot in time from a general FSI supersonic parachute simulation in Fig. 4 that displays the uniform and smooth pressure distribution extrapolated from the surrounding flow field. In addition, Alg. 1 describes the treatment that is provided to geometry elements that were not pierced during the x-ray tracing process, and thus do not have an associated irregular point/sampling cloud, so these elements must 'receive' an irregular point from their connectivity node neighbors.

Algorithm 1 Robust Flow Field Sampling

1. The x-ray tracing procedure is conducted, identifying pierce points and irregular points (see Fig. 3a).
2. Irregular points build full interpolation clouds via unit clouds[25] (see Fig. 3b).
3. All triangular, planar elements on the geometry representation that were pierced during the x-ray tracing propagate the irregular point that formed from their intersection to their node neighbors (see Figs. 5a-d).
4. All elements on the geometry representation that were not pierced during the x-ray tracing consider the irregular points propagated to them by their node neighbors and pick the closest one (that does not have a pierce point between itself and the candidate irregular point). This process is iterative — *i.e.*, the irregular point mapped to an element can change as different points are offered to it, and the elements that have an irregular point mapped to them from the pierced elements now provide this irregular point to their node neighbors (see Figs. 5a-d).
5. With the irregular point - geometry element mapping complete, interpolation coefficients are computed via WLSQR techniques based on difference of the element centroid position and the location of the points in the full interpolation clouds.
6. Primitive flow field quantities are computed at the face of the elements on the geometry representation (in preparation for being passed to the CSD solver as viscous and inviscid tractions).

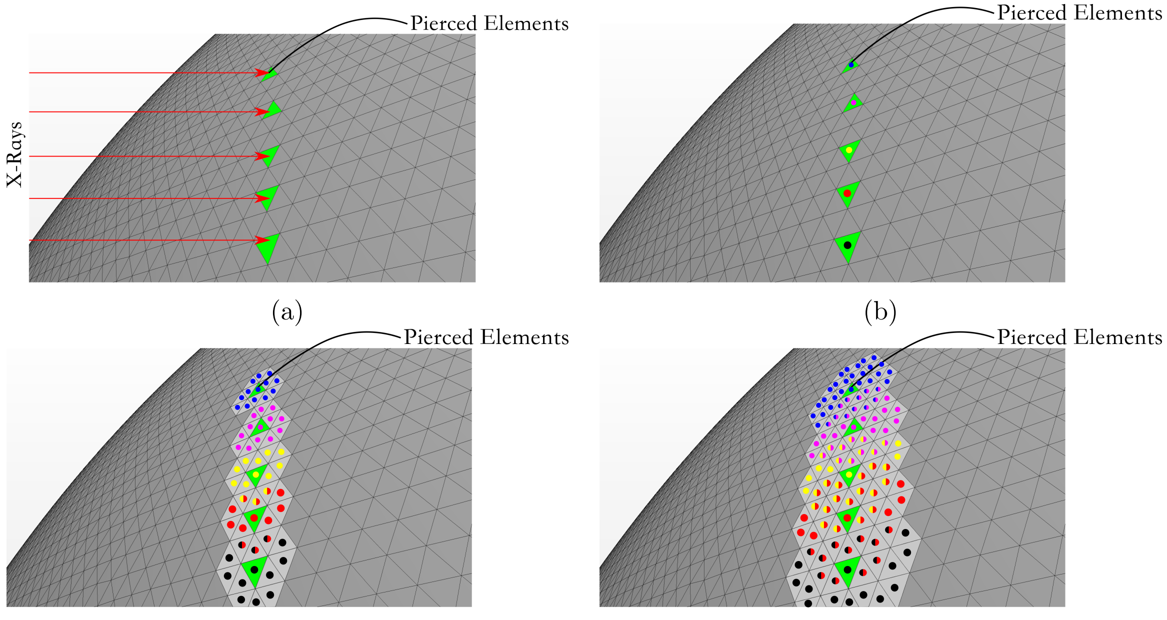

(a) (b)

(c) (d)

Figure 5: Illustration of (a) a selection of elements being pierced during the x-ray tracing process, (b) the pierced elements being associated with an irregular point (each color represents a different irregular point), (c) pierced elements propagating their associated irregular point to their connectivity node neighbors, and (d) the connectivity node neighbors propagating this irregular point to their connectivity node neighbors. Split colored elements have been offered multiple irregular points through the propagation iterations and must select the closest irregular point out of these.

2. Parallel Self-Contact Implementation

In simulations of inflation, the parachute geometry can undergo massive deformations, and certain topologies may see the parachute displace in such a way that parts of itself would pass through other parts of itself (*i.e.*, the region between two inflating gores has a high probability for contact). In reality, of course, the two contacting areas would 'contact' one another, exchange momentum, and not pass through one another.

While much research has been conducted on the proper way to enforce contact conditions into the governing equations,[34–36] and local neighborhood searches can be used to limit the search of possible contacting areas, the extension to high-performance, parallel computing is not always straight forward, or at least scalable. In these cases, the global information is partitioned across N_{CPUs} computers, and (usually) no one process knows the full set of global information. The options are usually to give the global information to all processors and have them do a local neighborhood search through hundreds of thousands of nodes on the geometry representation, which can be cumbersome, or to communicate information from process to process through the course of the simulation, where a communication bottleneck can be reached.

In this paper, a method is proposed that utilizes the efficient, fully parallel x-ray tracing program described earlier to identify and enforce contact in a structured Cartesian framework. The method is scalable, and each process can identify contact in the global domain and then uniquely enforce contact within its partition of the global domain. This is possible because each process is given access to the global triangulation of the geometry. Then, an x-ray passing through the domain can store the global ID of every element it intersects on the geometry and then only deal with identifying and enforcing contact with those triangles.

Note the method is especially advantageous because the framework needed to identify contact via the x-rays is already in place and necessary for geometry queries and other core aspects of the IBM. Thus, the only added cost is to implement some contact criteria on the results of the x-ray tracing to identify contact and the enforcement of contact through loading. The method that is conducted every timestep to identify and enforce contact is described in Alg. 2 and illustrated in Figs. 6a and 6b.

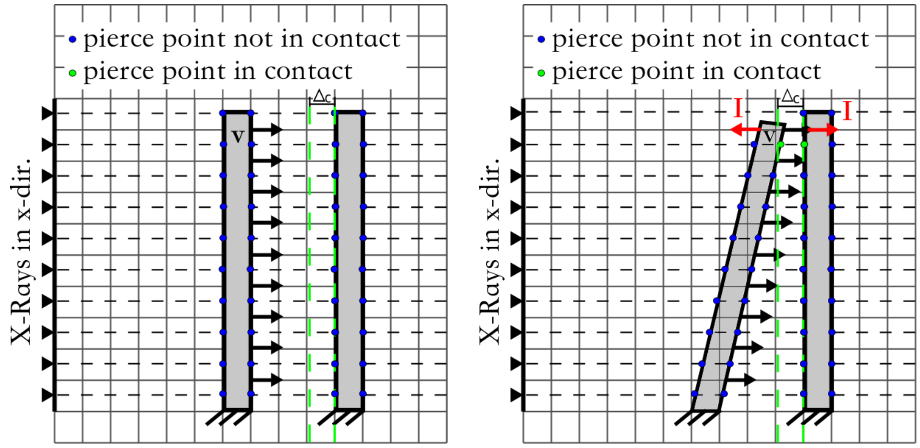

(a) (b)

Figure 6: (a) and (b) Illustration of two clamped plates contacting each other with a contact width Δ_c within a Cartesian framework. The left body is moving to the right with velocity v and the right body is stationary. Once the minimum distance between two pierce points gets smaller Δ_c, than contact is identified, an impulse is applied to the pierced elements using Eq. 12.

While the contact can be enforced in a variety of ways, in this work, frictionless contact is enforced in a very simple manner based off of the conservation of momentum and the linear-impulse momentum theorem. For a simple inelastic collision with a coefficient of restitution $\alpha < 1$ of an element A initially at velocity $\boldsymbol{v}_{A_i}$ with mass m_A and an element B initially at velocity $\boldsymbol{v}_{B_i}$ with mass m_B, the final velocities of the elements are given as

$$\boldsymbol{v}_{A_f} = \frac{\alpha m_B(\boldsymbol{v}_{B_i} - \boldsymbol{v}_{A_i}) + m_A\boldsymbol{v}_{A_i} + m_B\boldsymbol{v}_{B_i}}{m_A + m_B} \quad \text{and} \tag{11}$$

$$\boldsymbol{v}_{B_f} = \frac{\alpha m_A(\boldsymbol{v}_{A_i} - \boldsymbol{v}_{B_i}) + m_A\boldsymbol{v}_{A_i} + m_B\boldsymbol{v}_{B_i}}{m_A + m_B}.$$

Then, the impulse on each element, $\boldsymbol{I} = \int_t^{t+\Delta t} F dt$, necessary to enforce the contact conditions at time t over the course of a timestep of width Δt is given by

$$\boldsymbol{I}_A = \int_t^{t+\Delta t} m_A\ddot{\boldsymbol{x}}dt = \Lambda(t)m_A(\boldsymbol{v}_{A_f} - \boldsymbol{v}_{A_i}) \text{ and } \boldsymbol{I}_B = \int_t^{t+\Delta t} m_B\ddot{\boldsymbol{x}}dt = \Lambda(t)(\boldsymbol{v}_{B_f} - \boldsymbol{v}_{B_i}), \tag{12}$$

where the function $\Lambda(t)$ can be included to apply the impulse over a longer period of time than a single timestep. In the current work, the impulse is applied over the course of a single timestep.

In this work, because we are primarily interested in self-contact between regions of the same geometry, we assume that $m_A = m_B$, thus, the expressions for the final velocities after contact reduce down to a swapping of velocities between elements A and B, with some loss defined by α. While this enforcement of contact does not provide friction, its easy implementation into the parallel framework makes it appealing, and this method has been shown to adequately enforce a 'no penetration' condition on a variety of test cases in different flow regimes. A demonstration of the parallel contact algorithm is shown in Figs. 7a-f, where two flat plates clamped along the bottom edge are pushed into one another with equal pressure forces acting in opposite directions within a quiescent flow field. The contact is defined by a coefficient of restitution $\alpha = 0.75$.

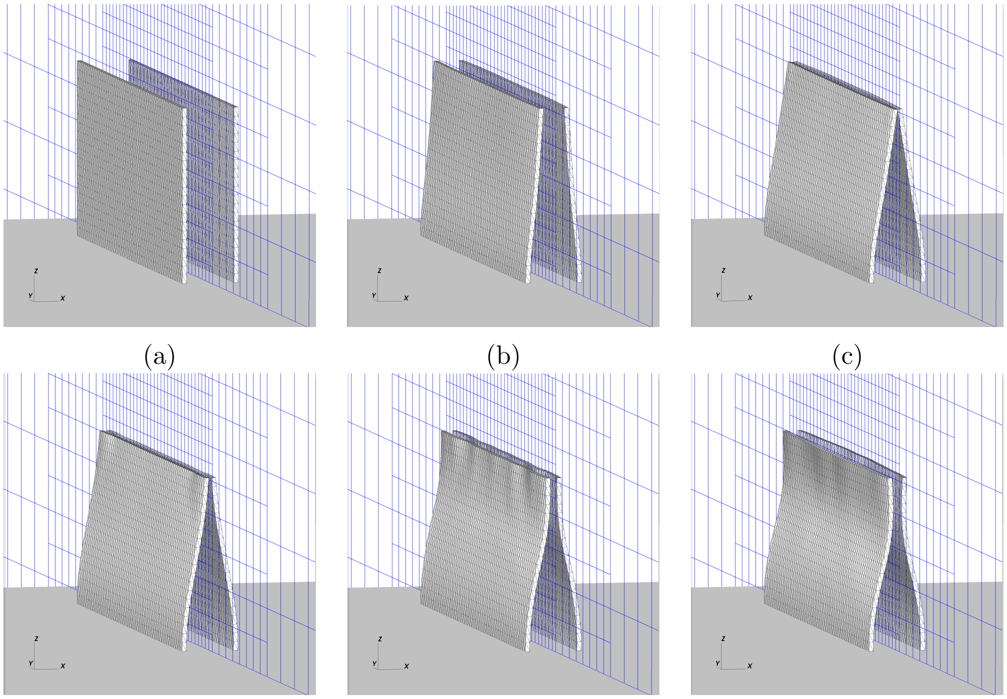

(a) (b) (c)

(d) (e) (f)

Figure 7: (a-f) Six snapshots in time from a simulation demonstrating the introduced parallel contact algorithm. In this case, two clamped plates in a quiescent fluid are forced into contact with one another via equal pressure forces acting in opposite directions.

Algorithm 2 Parallel Self-Contact Algorithm

```
The x-ray tracing procedure is conducted, identifying pierce points and irregular points (see Fig. 3a).
Each process checks the distance between pierce points that were identified during the x-ray tracing. Note that both of these pierce points do not have to lay inside the process's partition, thus, each process can identify contact between a surface in its partition and surfaces outside of its partition. Then, later, it is only responsible for enforcing contact to surfaces within its partition.
If the distance between two successive pierce points at time level $n$ (that are not on opposite sides of a shared thickness), $\Delta_{pp}$, is less than some pre-defined width of contact, $\Delta_c$, then possible contact is identified between the two elements associated with the pierce points.
To determine if contact is expected to occur within the next timestep, a prediction step is done on the gap size between the two pierce points that are in possible contact. The two associated elements compute the distance that they will travel in one timestep based on their current body velocity and the simulation timestep size to compute the estimated gap size at time level $n+1$, $\tilde{\Delta}_{pp}^{n+1}$. Then, if $||\Delta_{pp}^{n}|| < ||\Delta_c||$ and $||\tilde{\Delta}_{pp}^{n+1}|| < ||\Delta_{pp}^{n}||$, the two elements are identified as in contact. In other words, if the elements are sufficiently close, and the gap between them is closing, they are in contact and require forcing so they do not penetrate one another.
The impulse on the elements is computed via Eq. 12 assuming $m_A = m_B$.
This impulse is added in addition to the usual fluid dynamic forces in the global traction vector that is provided to the CSD solver, thus, the CSD implicitly enforces contact based on the position of the geometry representation.
```

3. Porous Media Interface Condition

The materials used for the broadcloth of parachute canopies, due to their fabric weave manufacturing, are permeable. It was shown during the 1960's and 1970's that the stability of a DGB parachute was a function primarily of porosity and Mach number,[1] thus, any computational FSI method considering high-fidelity simulations capable of performance prediction must include a method for representing flow through the permeable canopy broadcloth. In a conventional CFD method, the porous medium would be modeled by fully resolving the thickness of the medium and adding a source term to the momentum equations. The source term essentially acts as a pressure gradient against the flow, providing resistance. This follows the well-known Darcy's law for a porous medium (for incompressible fluids) and is simply derived from the conservation of momentum. The flow rate, Q, through this medium is proportional to the pressure difference across the medium, Δp, and is given as

$$Q = \frac{K_p \Delta p}{\mu L}, \tag{13}$$

where L is the thickness, K_p is the permeability of the porous medium, and μ is the kinematic viscosity of the fluid. For compressible flows, the continuity equation, which in 1-D simplifies to

$$\dot{m} = \rho u = \text{const.}, \tag{14}$$

where $\dot{m}$ is the mass flow rate of the fluid, ρ is the density of the fluid, and u is the velocity of the fluid, needs to be considered as well, potentially with the energy equation and a fluid equation of state (here, the ideal gas law).

A scenario where a conventional source term model would be used is represented in the top illustration of Fig. 8a, where flow is passing through a finite-thickness porous medium in a channel, and the porous medium is represented by the grey-shaded region. Reiterating from the previous sections, however, to maintain multiple Cartesian cells within the thickness of the parachute geometry is computationally prohibitive given the small thickness of a parachute fabric. So in line with previous developments from this work and past works, a method is developed for representing the permeability of the parachute fabric assuming *a priori* that the parachute fabric cannot be resolved considering the large difference in the thickness of the parachute fabric and the minimum grid spacing used in the computational domain.

Following the developments in the past sections, in the current, sharp IBM, the boundary conditions are applied at the surface of an immersed boundary. Consistent with this approach, a porous medium interface condition will be applied directly at the pierce points. Then, the flux finite difference stencils at the irregular points will include the interface flux, which depends on the state vector from both sides of the porous

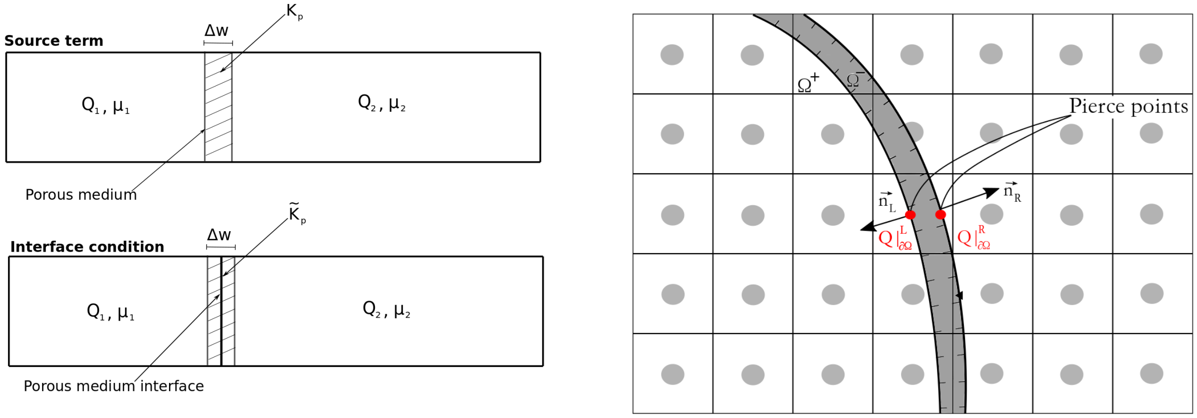

(a) (b)

Figure 8: (a) Illustration of a (top) conventional source term approach to model a porous medium and (bottom) the newly developed interface method approach for geometries much smaller than the minimum grid spacing in the fluid domain and (b) a schematic of a thin, 2D geometry, $\partial\Omega^-$, immersed in a structured Cartesian domain, $\partial\Omega^+$, being pierced during the x-ray process and a pair of elements defined by the 'left' and 'right' face geometric normal vectors, $\vec{n}_{L,R}$, exchanging the state on their side of the immersed interface $(Q|_{\partial\Omega}^{L,R})$ with one another.

medium. In this way, the porous medium is represented as a possibly infinitesimally thin interface condition, rather than being fully (or partially) resolved and represented as a source term (though in this work, the interface will always have a very small, but finite physical thickness, see Sec. IV). This is illustrated in the bottom image from Fig. 8a.

The porosity interface condition used in the current implementation could be based on any arbitrary complex source term model currently available for porous medium modeling, such as provided in Schmidt,[37] which can be written (here, in 1-D form) as

$$\rho S = f\left(\dot{m}, \dot{m}^2, K_p, \epsilon, \overline{d}, Re_{\overline{d}}, ...\right), \tag{15}$$

where the source term is commonly a nonlinear function of the massflow rate $\dot{m}$ and some porous medium modeling parameters, for example the permeability, porosity, the Ergun coefficient, the mean particle size for the porous material, $\overline{d}$, the porous medium Reynolds number, $Re_{\overline{d}}$, *etc.* (see for example Ref. 37, which considers a drag coefficient, C_D, of the porous material for compressible flow).

In the current work, our porous media model is simply based on the Darcy-Forchheimer law, represented here in terms of a conventional source term model with source $\vec{S}_F$,

$$\vec{S}_F = -\frac{\mu}{K_p}\vec{v} - \beta|\vec{v}|\vec{v}, \tag{16}$$

where μ is the dynamic viscosity, K_p is the permeability of the porous medium, β is the inertial permeability of the porous medium, and $\vec{v}$ is the flow velocity vector. This source term can be equivalently expressed as the pressure drop across the porous medium as $\partial p/\partial n$, and Eq. 16 can then be expressed as

$$\frac{\partial p}{\partial n} = -\frac{\mu}{K_p}v_n - \beta v_n^2, \tag{17}$$

where the normal velocity v_n is obtained by the dot product between the porous medium geometric normal vector, $\vec{n}$, and the fluid velocity vector, $\vec{v}$. Eq. 17 governs the pressure jump across the porous material interface and can be solved numerically considering the conservation of mass and energy as well as the ideal gas law. In order to simplify the solution procedure, the energy equation was replaced by assuming a linear temperature variation across the interface. To enforce this interface condition at pierce points across the surface of the parachute, the process listed in Alg. 3 is employed.

Algorithm 3 Porous Media Interface Treatment

```
1: The x-ray tracing procedure is conducted, identifying pierce points and irregular points (see Fig. 3a).
2: A representation of the geometry with a 'one-to-one' matching of elements on the front and back sides of the parachute broadcloth is employed, where elements on either side are paired together. In other words, the parachute is a finite thickness geometry with both discretizations of the major faces being mirror images of one another such that each element on one side has a 'pair' through the thickness of the geometry. (see Fig. 8b)
3: Pressure and temperature, and density (from the ideal gas law), are obtained at the immersed boundary via methods similar to those introduced in Alg. 1.
4: An element pierced during the x-ray tracing procedure is used in the enforcement of the porosity interface boundary condition. Thus, these elements are required to exchange the state of the flow from its 'side' with that of its pair on the other side of the porous medium (through the thickness of the geometry).
5: The mass flow rate through the porous medium is obtained by solving Eq. 17 assuming conservation of mass, a linear variation of temperature, and using the thermodynamic state, i.e., pressure, temperature and density, on both sides of the porous medium. Following the basic principle of conservation of mass, the mass flow rate is then used to fully prescribe the state vector on both sides of the medium.
6: Flux derivatives at irregular grid points are formed following the sharp IBM approach (here, for the x-direction) with $\frac{\partial \vec{F}}{\partial x}|_{i,j,k} = c_i^{(\partial\Omega)} \vec{F}^{\pm}(Q|^{L}_{\partial\Omega}, Q|^{R}_{\partial\Omega}) + \sum_{m=1}^{N} c_i^{(m)} \vec{F}^{\pm}_{i+k,j,k} + \mathcal{O}(\Delta x^p)$, where $\partial\Omega$ represents the immersed boundary (or pierce points), $c_i$ are finite-difference stencil coefficients, $N$ is the number of Cartesian grid points included in the irregular point stencil, and $Q|^{L,R}_{\partial\Omega}$ is the left and right state of the flow at the immersed porous medium interface.
```

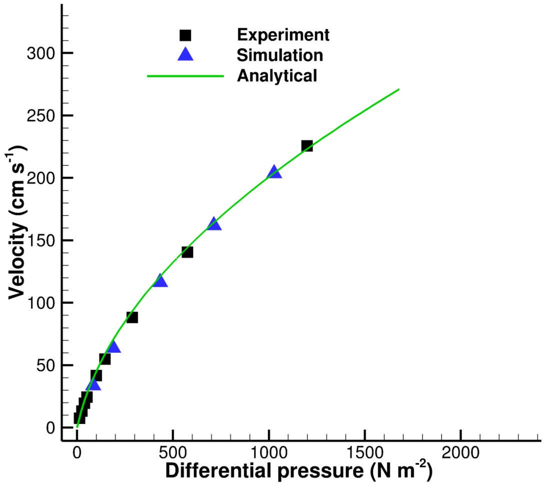

Figure 9: Comparison of experimental results from Cruz *et al.*[38] and simulations from the current work considering the measured permeability of PIA-C-7020D Type I parachute broadcloth.

To evaluate the formulation and implementation of the porous media interface condition, experiments by Cruz *et al.*[38] considering the PIA-C-7020D Type I parachute broadcloth used in the ASPIRE SR01 mission are reproduced. In the experiments, a device is used to supply various pressure differentials across samples of the broadcloth, and the resultant porosity is measured. To recreate this experimental setup with simulations, a 2D, slip wall channel domain with a porous medium specified in the middle and a uniform velocity profile inflow, similar to that seen in Fig. 3, is considered. In these simulations, the state variables at the left and right sides of the interface are chosen to provide pressure differences across the porous medium similar to those considered in the experiments. The results of these simulations for the interface method and the analytical formulation in Eq. 17 are compared against experimental results in Fig. 9. As shown, all simulations are in excellent agreement with the experimental results.

In addition to this, to test the qualitative differences observed in the flow field when considering a porous broadcloth in conditions relevant to supersonic parachute inflation, a $M = 2.0$ flow field is developed over a static, ‘as manufactured’ parachute geometry for an impermeable parachute and one considering the porous media interface condition. The results from these simulations are shown in Figs. 10a-d. It can be seen that the pressure difference across the leading and trailing faces of the parachute canopy is smaller when the porous media interface condition is considered. As some flow is allowed to pass through the broadcloth, the velocity in the wake of the canopy is also larger for the case with porosity in comparison to the impermeable parachute. This rise in flow velocity in the wake of the parachute and the drop of the pressure are necessary to maintain a constant mass flow rate through the porous medium. It can also be seen that the case with the porous media interface condition has a bow shock that rests slightly closer to the parachute canopy than the impermeable case. This is also due to the decreased pressure drop across the canopy and the presence of flow that passes through the broadcloth. These qualitative findings are expected to be much more dramatic as the porosity increases.

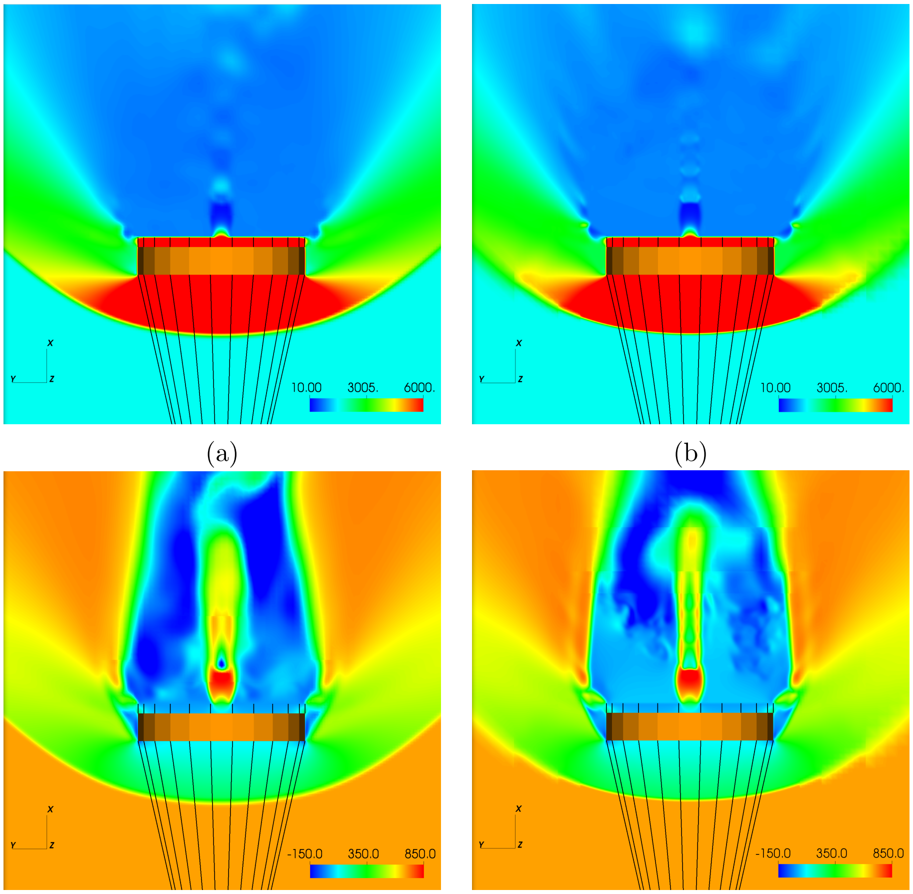

(a) (b)

(c) (d)

Figure 10: (a) Saturated color contours of the pressure field (Pa) in the fluid and the static parachute geometry with an impermeable parachute and (b) with a porous media interface condition. (c) Saturated color contours of the streamwise velocity (m/s) and the static parachute geometry with an impermeable parachute and (d) with a porous media interface condition.

4. Adaptive Mesh Refinement

The block structured Cartesian IBM was also extended to consider adaptive mesh refinement (AMR) capabilities in order to track criteria relevant to supersonic parachute inflation: (1) the formation and evolution of discontinuities in a compressible flow field, notably, the bow shock upstream of a parachute canopy in supersonic flow, and (2) the arbitrarily large displacements of a complex geometry, *i.e.,* the inflating parachute canopy. Criteria (1), or flow feature refinement, is performed by measuring the maximum pressure gradient within all of the Cartesian blocks in the domain and then refining the blocks that observed a pressure

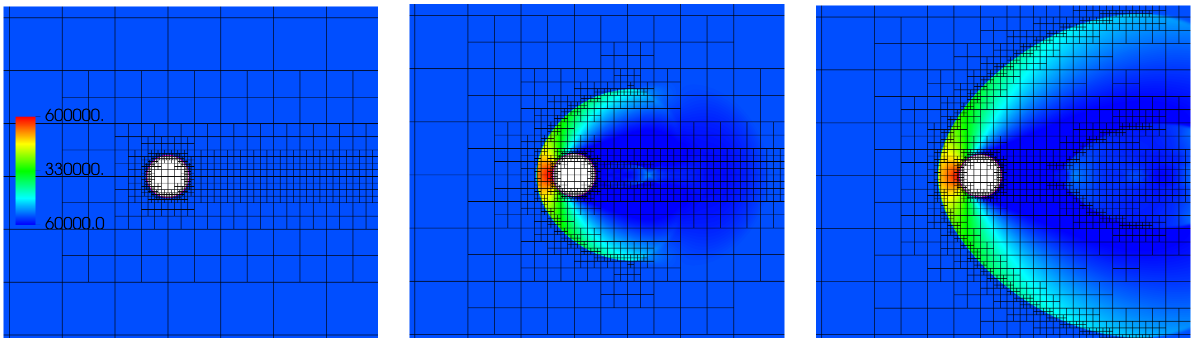

(a) (b) (c)

Figure 11: (a-c) Snapshots in time of the pressure field (Pa) from a simulation of a developing supersonic flow with $M = 2.0$ over a 2D sphere using a flow feature refining Cartesian mesh.

gradient within some percent of the maximum pressure gradient in the flow field to the second finest level. Coarsening from the second finest level is performed when the pressure gradient in a previously refined block drops below some percent of the maximum pressure gradient in the flow field, or in other words, when the flow features of interest are no longer in this block. This process is demonstrated in Figs. 11a-c on a 2D sphere in a developing supersonic flow field with Mach number 2.0. Additional details about octree-data structure used to organize the mesh and the flow feature tracking strategy are provided in Browne *et al.*[39]

The finest grid level is used for criteria (2), *i.e.*, geometry tracking. Refinement to the finest level is performed on a block when an element on the geometry representation lies within the volume of the block. Coarsening from the finest level is performed on a block when there are no elements of the geometry representation within the volume of the block. This process is demonstrated in Figs. 12a-c on a 2D sphere moving in a circular arc in a supersonic flow field with Mach number 2.0, using the flow field and block arrangement from Fig. 11c as the initial condition for the simulation.

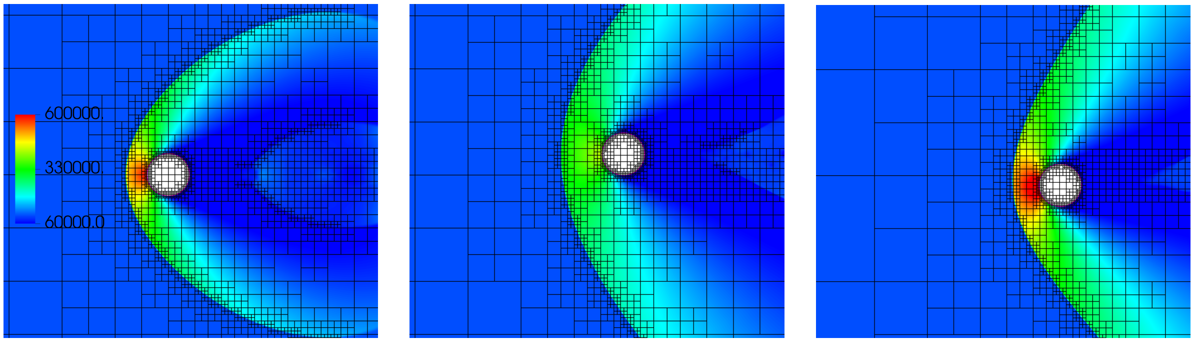

(a) (b) (c)

Figure 12: (a-c) Snapshots in time of the pressure field (Pa) from a simulation of a supersonic flow with $M = 2.0$ over a moving circle using a flow feature refining and geometry tracking Cartesian mesh.

B. Finite Element Formulation

Although membrane elements are often used in the simulation of parachutes, membrane elements derived from tension-field theory[40] are unable to properly capturing wrinkling due to the lack of flexural rigidity. These elements form an infinite number of wrinkles across a surface with no bending stiffness when subjected to a compressive loading, and when a membrane is in a slack state, or in the presence of no loading, the configuration of the membrane is not defined.[41] A small amount of bending stiffness is necessary to determine the formulation and distribution of wrinkles.[42] While there are methods intended to model wrinkling in membranes,[41, 43] and despite the locking phenomenon present in thin shell formulations here, a thin shell element is employed due to their generality when applied to various thin structures.

This locking phenomena in a thin shell element occurs when a given element formulation is unable to satisfy Kirchhoff's constraints that a line initially straight and perpendicular to the mid-plane of the shell remains straight and perpendicular to the mid-plane after deformation — as well as maintain a constant thickness throughout the shell. That is, the element formulation does not provide zero (or at least very small) transverse shear strains and negligible shear deformations. This is usually sensitive to the thickness of the shell element, and the locking is ultimately worsened as the thickness of the shell decreases.[44] There have been many methods proposed to alleviate the locking phenomena, the two most popular of which are reduced[45] and selective[46] integration and assumed strain variations. One of the key issues with the reduced and selective integration methods is the lack of theoretical explanation, in addition to the presence of spurious zero energy modes.[47] A variation of the assumed strain variation approach is the Mixed Interpolation of Tensorial Components,[44, 48–50] which has been applied to many triangular and rectangular shell and plate elements to alleviate locking. The most commonly used shell element from this family is the MITC4 rectangular shell element, but rectangular elements are shown to have less than optimal convergence properties when distorted.[50, 51] Because of the highly complex geometries expected to occur during parachute inflation, and the ease of generating a triangulation for a complex topology, the MITC3 triangular shell element is chosen to discretize the parachute canopy in this work. In addition, to simulate the suspension lines in the parachute model, a geometrically nonlinear cable finite element formulation as described by Bathe[48] was implemented and coupled to the MITC3 shell elements. Validation of the CSD solver and the details for unsteady analysis can be found in Refs. 24 and 28.

IV. CFD-CSD Coupling

A. Coupling Algorithm

The CFD and CSD solvers are coupled together in a weak fashion. The unstructured, infinitesimal thickness CSD mesh is wrapped by an unstructured representation of the geometry with a physical thickness. In other words, the CSD mesh is the mid-plane of the surrounding geometry representation. The parachute suspension lines are not wrapped in a geometry representation, thus, the CFD solver does not 'see' them. The geometry representation acts as the interface between the two solvers: the CFD solver provides loads to the geometry representation, the CSD solver obtains these loads from the geometry representation, the CSD solver displaces the geometry representation, and the CFD solver is advanced with the new geometry representation. This procedure is summarized in Fig. 13. In this way, the solution procedure is partitioned, or staggered, and the coupling is so-called weak because this process is done once per timestep. More details on the coupling of the two solvers can be found in Boustani *et al.*,[24] and the extension to consider parallel CFD-parallel CSD coupling in Boustani *et al.*[28]

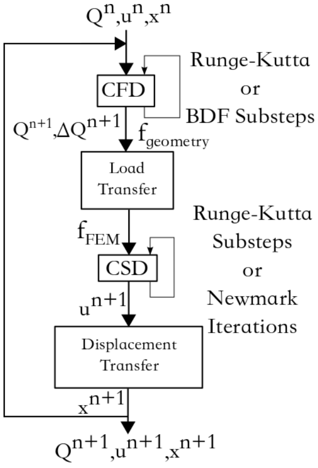

Figure 13: Flowchart for the coupling approach used in the current research where **Q** is the flow state vector, **u** is the structure state vector, and **x** is the position of the shared boundary.

Because the contact algorithm described by Alg. 2 involves both solvers, the identification and enforcement of contact can be thought of as modifying the flowchart in Fig. 13 slightly. The identification of contact can be added as an intermediary step before the CFD solve, and the enforcement of contact can be added before the load transfer, where the contact tractions are added into the fluid dynamic tractions that were obtained on the geometry representation. The CSD solver then implicitly enforces contact on the geometry representation as it advances the solution with the combined contact and fluid dynamic tractions.

V. Results

The recent developments to the computational FSI method such as improved flow field sampling, self-contact, the porous media interface condition, and adaptive mesh refinement on the canopy will be investigated and demonstrated on the deployment of a 24-gore $0.8m$ diameter disk-gap-band (DGB) parachute in supersonic conditions resembling the upper Martian atmosphere that was also considered by Boustani *et al.*[28] The fluid, structural, and geometric properties are chosen in accordance with experiments by Sengupta *et al.*[8] and simulations by Karagiozis *et al.*[12] and Yu *et al.*,[20] where a sub-scale model of the heritage Viking parachute and capsule are considered. A schematic of the capsule is shown in Fig. 14a, and the total parachute system is summarized in Fig. 14b.

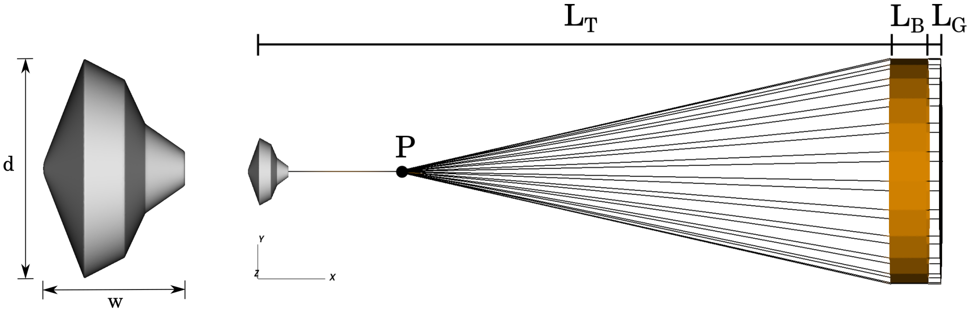

(a) (b)

Figure 14: (a) Drawing of the sub-scale Viking capsule used in this research (w = $0.1072m$, see Ref. 12) and (b) schematic of the parachute system used in this research. The marked distances are: the non-dimensional trailing distance from the leading edge of the band to the mid-plane of the capsule $L_T = x/d = 10.6$, where x is the dimensional trailing distance, the height of the band $L_B = 0.121D_0$, and the height of the gap $L_G = 0.042D_0$. Adjusted from Yu *et al.*[20]

The fluid and structural properties match those used in both the prior experiments and simulations and are summarized here. The Reynolds number is given as, $Re = \rho_\infty u_\infty d/\mu_\infty = 10^5$, with a fluid density of $\rho_\infty = 0.0184527kg/m^3$, a free stream velocity of $u_\infty = 688.69m/s$, and dynamic viscosity of the ambient fluid μ_∞ computed with Sutherland's law at a temperature of $T_\infty = 294.93K$. The capsule diameter is given here as $d/D_0 = 0.21$, and $D_0 = 0.8m$ is the nominal diameter of the parachute. The Mach number is given as, $M = u_\infty/c_\infty = 2.0$, where c_∞ is the speed of sound in the ambient fluid. The elastic modulus of the parachute material is $E = 878MPa$, Poisson's ratio is $\nu = 0.33$, the thickness of the parachute material is $h = 6.35 \times 10^{-5}m$, and the density of the parachute material is $\rho_p = 614kg/m^3$. The suspension lines have a diameter $d_c = 0.99 \times 10^{-3}m$, elastic modulus $E = 43GPa$, and linear density $\rho_c = 8.27 \times 10^{-4}kg/m$.

For the simulation results shown here, the extent of the computational fluid domain is $[-6.25D_0, 6.25D_0] \times [-6.25D_0, 6.25D_0] \times [-6.25D_0, 6.25D_0]$. The left boundary was treated as an inflow boundary, the right boundary was treated as a supersonic outflow boundary, and the side boundaries were treated as far-field boundaries. The minimum grid spacing for the base case was $\Delta x_{min} = \Delta y_{min} = \Delta z_{min} = D_0/164$. The total number of grid points in the CFD domain after flow fields were developed utilizing AMR was approximately 10 million. A flow field is developed over a static parachute geometry to allow transients to convect out of the domain and to establish the bow shock ahead of the canopy, and ahead of the capsule for the cases that consider the capsule. In addition, for cases considering AMR, this flow field run also initializes the arrangement of the Cartesian blocks for the FSI simulations, notably the blocks that are tracking the bow shock ahead of the parachute canopy. These initial flow fields are shown in Figs. 15a and 15b with the Cartesian block arrangement at $\Delta x_{min}/2 = \Delta y_{min}/2 = \Delta z_{min}/2$. Note, each block contains $8 \times 8 \times 8$ grid points. The suspension lines are discretized with 600 geometrically nonlinear cable elements in the CSD solver and are fixed at point P (see Fig. 14), and the parachute band and disk are discretized with 180,000 geometrically nonlinear MITC3 shell elements in the CSD solver. The phantom geometry representation is discretized with 400,000 flat, triangular elements in the CFD and CSD solvers.

A topological view of the inflated parachute canopy from experiments by Sengupta *et al.*[8] (image adjusted with permission from Witkowski *et al.*[52]) and from a general simulation in the current work is shown in Figs. 16a and 16b. This topological shape is in great qualitative agreement with the topology of the sub-scale

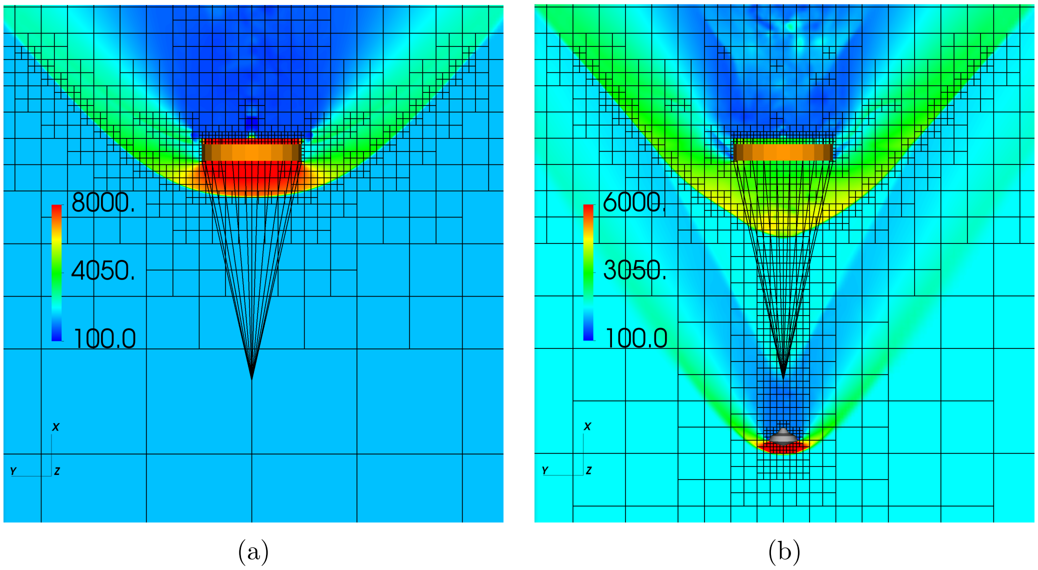

Figure 15: Color contours of the pressure field (Pa) and block arrangement of the developed flow field used as the initial condition for the FSI simulations (a) without the leading Viking capsule and (b) with the leading Viking capsule. Note, each block contains $8 \times 8 \times 8$ grid points.

MSL parachute presented by Witkowski *et al.*[52] The band and disk show very similar inflated shapes — the bands from the experiment and the simulations are both missing the characteristic bulge associated with DGB parachutes. The disks also show characteristic valleys along the radial seams with inflated material in between. In general, the case without the leading Viking capsule undergoes a very symmetric and uniform inflation. In the case considering the leading Viking-type capsule, rich dynamics are undergone by the parachute canopy before inflation as the leading canopy bow shock interacts with the wake of the bluff capsule. Notably, a partial collapse of the parachute band can be seen in Fig. 17, which is commonly observed in DGB parachutes operating above M = 1.5.[8] Following this dynamically rich inflation period induced by the turbulent wake of the capsule, a similar inflated shape is obtained.

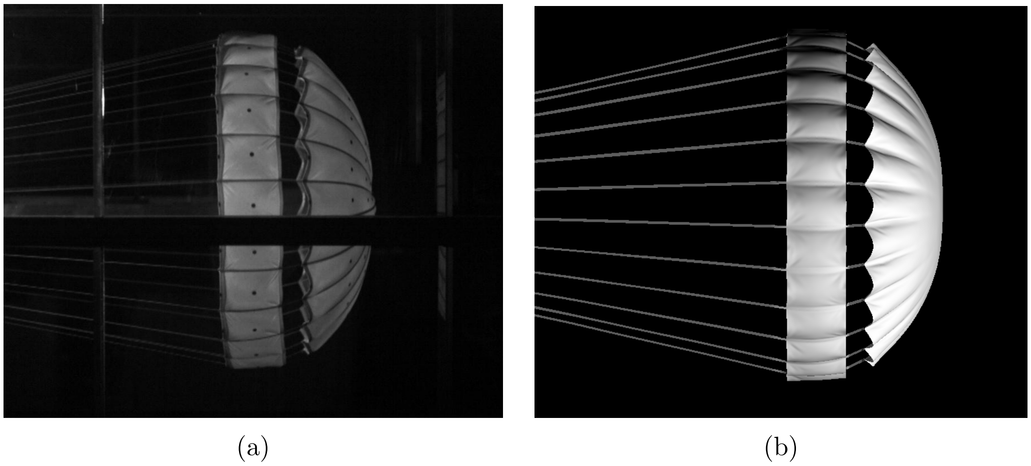

Figure 16: (a) Topological view of the inflated DGB parachute canopy from experiments by Sengupta *et al.*[8] (image adjusted with permission from Witkowski *et al.*[52]) and (b) from simulations conducted in the current work.

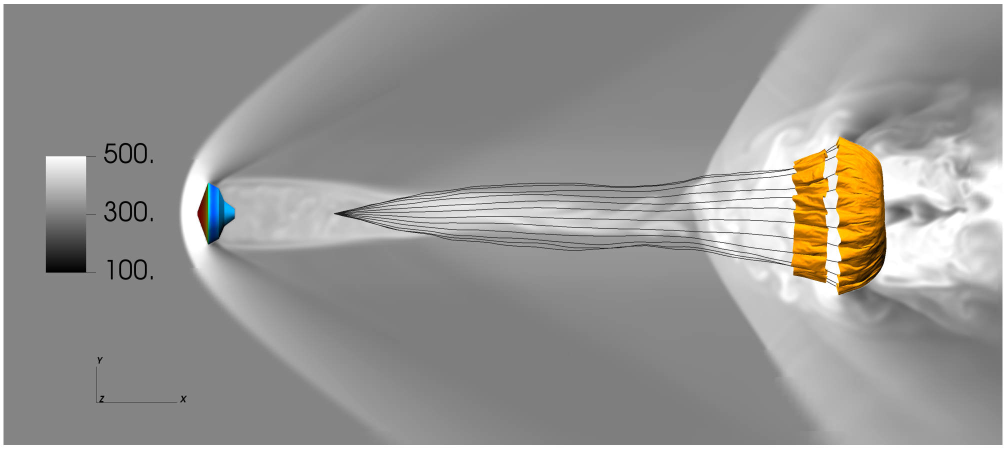

Figure 17: The partial collapse of the band observed during a general simulation considering the leading Viking capsule in color contours of the fluid temperature field (K). Pressure contours are shown on the Viking capsule.

The parachute is first considered without the leading Viking-type capsule as a simplified test bed to demonstrate and evaluate the aforementioned developments. The flow field, stress distribution on the canopy, and cable tension are presented and discussed. The stress distribution and cable tension (and ultimately the total force coefficient and coefficient of drag) are expected to become highly relevant quantities in future works that will focus on providing physical insight into the inflation process and performance prediction.

Instantaneous snapshots of the fluid pressure field at six instances in time can be seen in Figs. 18a-f along with the inflating parachute geometry. It can be seen that the bow shock and block arrangement are fully developed at the start of the simulation because of the use of the flow field from Fig. 15a as the initial condition of the flow field in the FSI simulation. The structural solver starts the simulation in an ‘as constructed’ shape and in a stress-free state. Thus, there is an initial adjustment phase in Figs. 18a and 18b where the band inflates due to the pressure difference across it, and the disk slowly starts to convect downstream as it is exposed to the freestream. It is common knowledge that an FSI solution is highly dependent on the initial state of the CFD and CSD solvers, and the initial topology and state considered here, while being a simplified test bed for demonstration and method development, is not representative of a parachute during actual inflation. Hence, more consideration will be taken when investigating initial conditions for both the CFD and CSD solvers as the method is applied to consider real-world flight tests, such as the ASPIRE missions.

In Figs. 18c and 18d, the canopy is contracting as it moves downstream and line stretch and peak cable tension occurs. By Fig. 18e, the canopy diameter is much smaller than it was at the start of the simulation, and the canopy’s downstream motion that was abruptly stopped by the line stretch causes the suspension lines to react and be driven inward. The canopy at this time, however, is starting to re-inflate and move outward. This time frame is when the most extreme self-contact was observed to occur as inflating gore slices are now in a much smaller diameter than at the start of the simulation, and adjacent gore slices contact one another as they inflate. Finally, by Fig. 18f, the canopy has established an inflated shape, but it is still subject to smaller-scale, oscillatory transient motion.

The same trends are observed in Figs. 19a-f where the streamwise velocity is shown with the von Mises stress distribution on the parachute canopy throughout the simulation. The von Mises stress represents the magnitude of the deviatoric strain energy, and it is used in structural analysis to reduce the deviatoric stress field down to a single scalar value that can be used for prediction of material failure, so it is a relevant quantity to measure when considering simulations of supersonic parachute inflation.

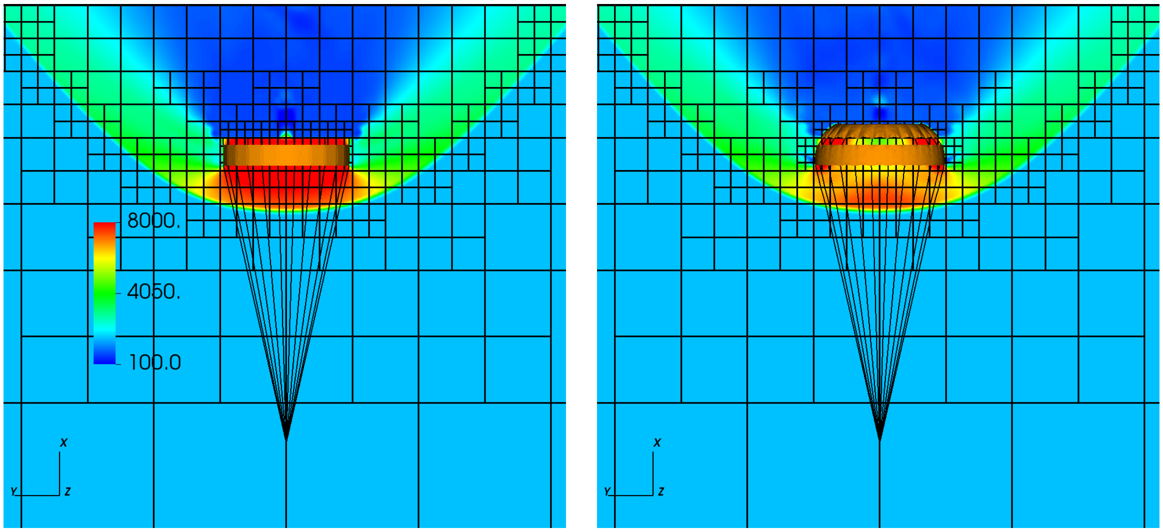

(a) 0.08 ms (b) 0.86 ms

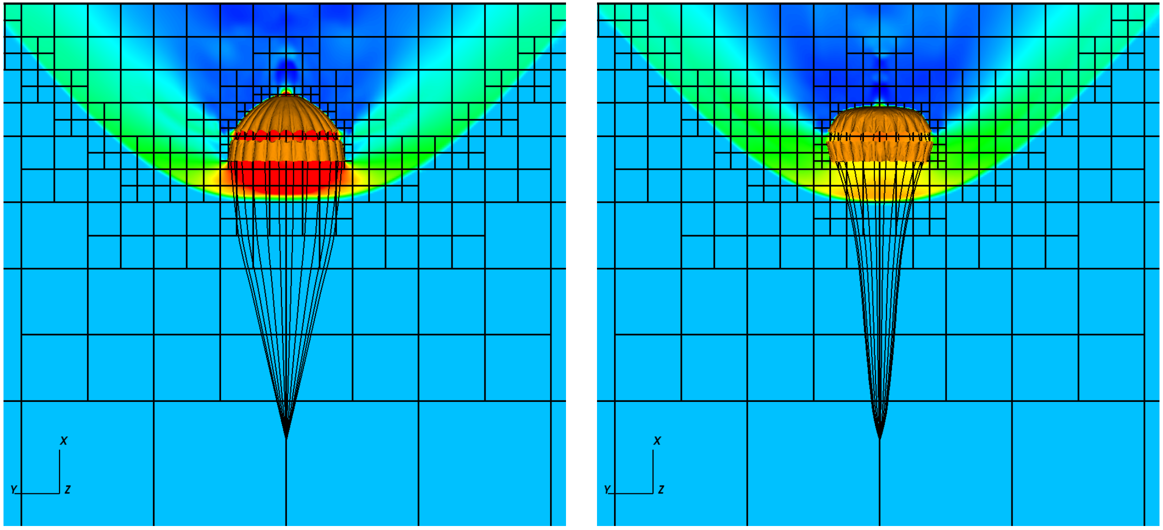

(c) 2.75 ms (d) 3.87 ms

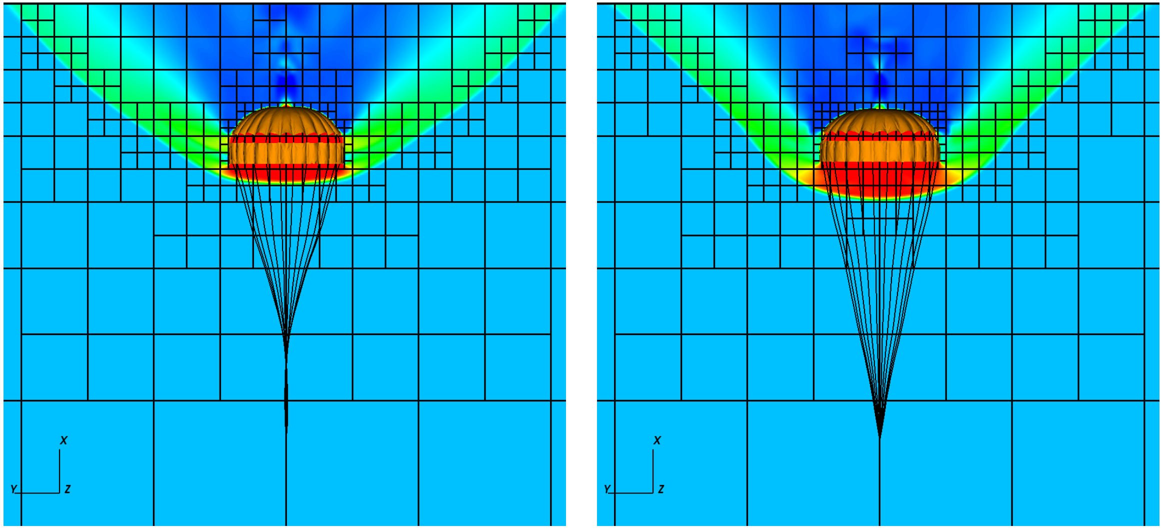

(e) 5.33 ms (f) 6.45 ms

Figure 18: (a-f) Color contours of the pressure field (Pa) in the flow field and the parachute geometry at six instances in time for a parachute without the leading capsule at freestream M = 2.0.

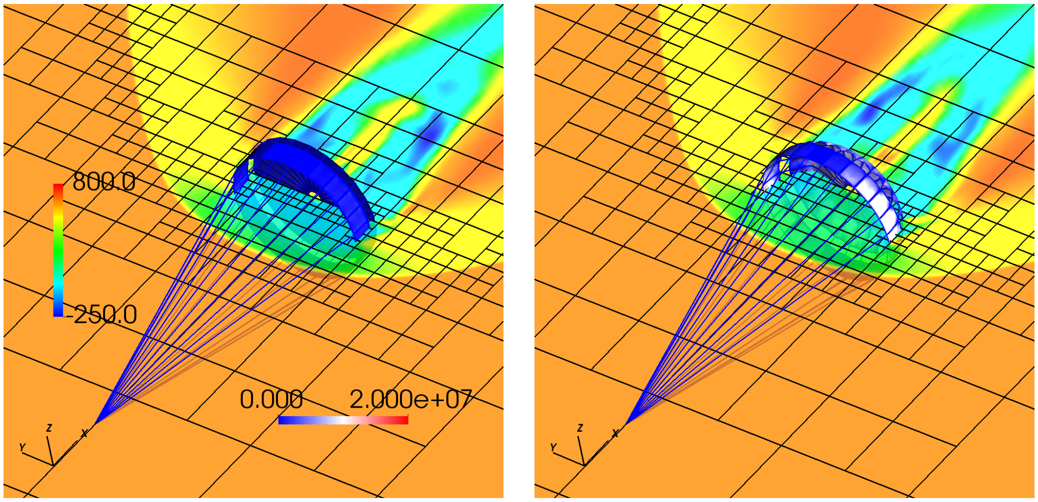

(a) 0.08 ms (b) 0.86 ms

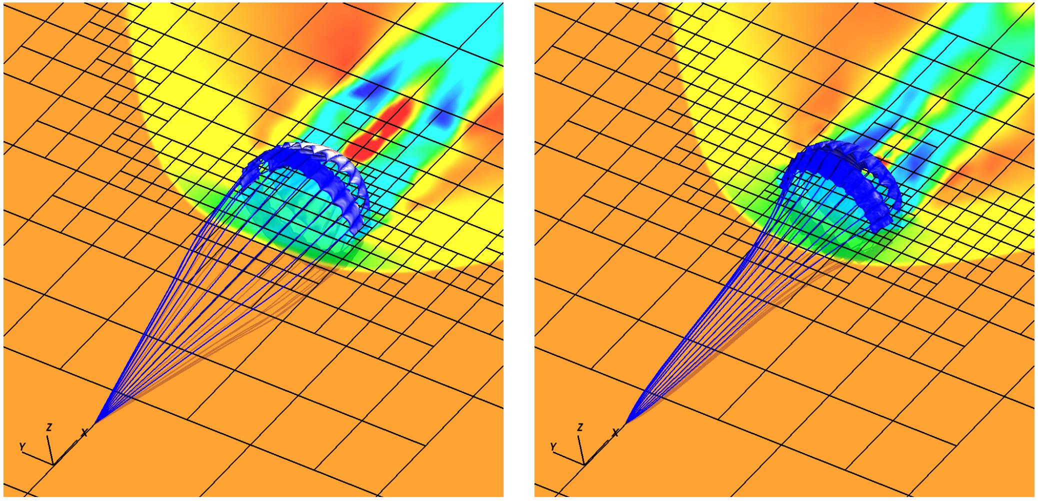

(c) 2.75 ms (d) 3.87 ms

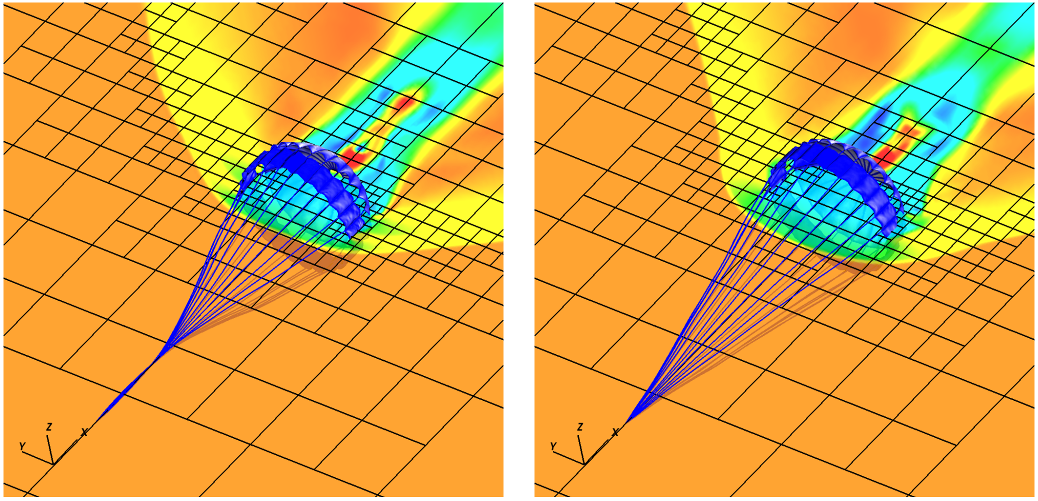

(e) 5.33 ms (f) 6.45 ms

Figure 19: (a-f) Color contours of the streamwise velocity (m/s) in the flow field (rainbow legend) and the von Mises stress distribution (Pa) on the parachute canopy (blue-red legend) at six instances in time for a parachute without the leading capsule at freestream M = 2.0.

Following this, the same sub-scale DGB parachute is considered with the leading Viking capsule upstream of the canopy. The presence of this capsule provides an asymmetrical and highly unsteady velocity profile to the inflating parachute canopy, in comparison with the symmetrical and uniform profile without the capsule. This results in rich dynamics during inflation. It is expected, however, that the final inflated shape will be similar to the case without the Viking capsule. Instantaneous snapshots of the streamwise velocity and the inflating parachute geometry at six instances in time from this case can be seen in Figs. 20a-f. As can be seen, despite a more dramatic contraction of the band during inflation, and an unsteady interaction between the wake of the capsule and the canopy bow shock, the resultant canopy topology is similar to the case without the capsule.

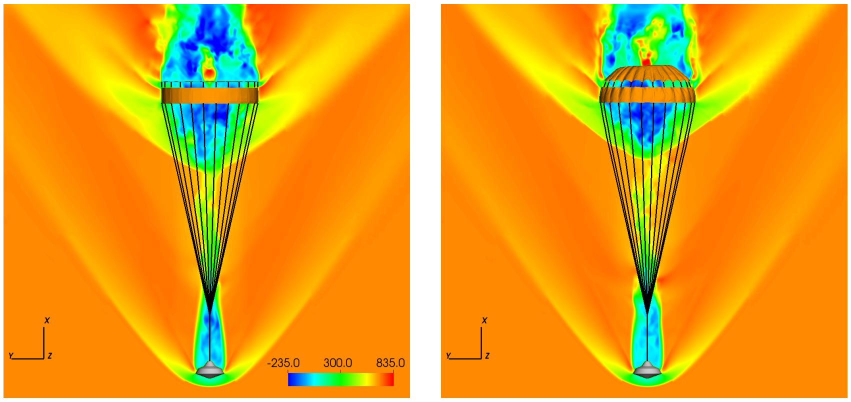

(a) 0.15 ms (b) 1.53 ms

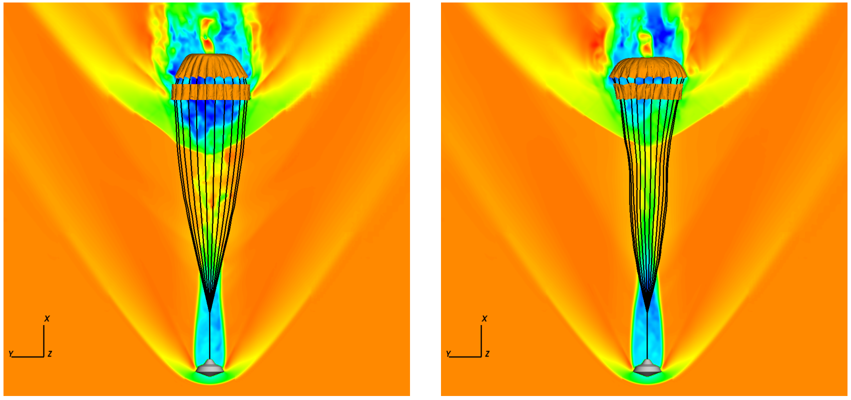

(c) 2.91 ms (d) 4.89 ms

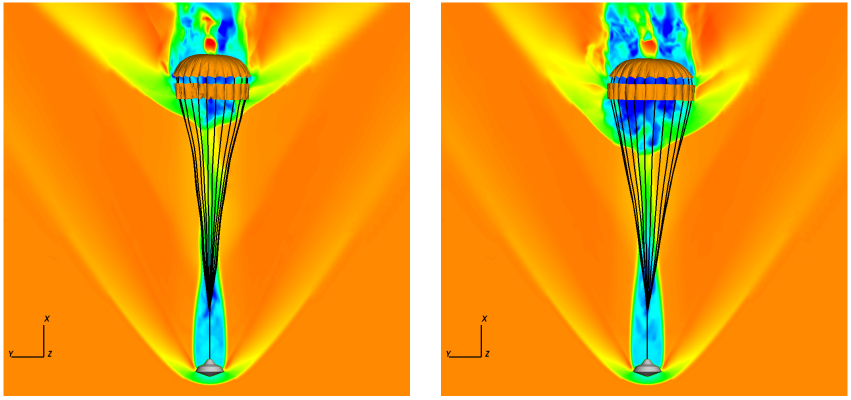

(e) 6.27 ms (f) 8.57 ms

Figure 20: (a-f) Saturated color contours of the streamwise velocity (m/s) in the flow field and the inflating parachute geometry and suspension lines at six instances in time for the case with the leading capsule inflating at freestream M = 2.0.

A quantitative comparison of the two cases (with and without the leading capsule) can be observed, however, in Fig. 21. The total tension in the 24 suspension lines from each case is plotted as a function of time in Fig. 21. It is evident that the inflation time for the case without the upstream Viking capsule is longer than that for the case without the capsule. This is attributed to the capsule breaking up the uniform freestream velocity profile and inducing a smaller streamwise velocity in the wake of the capsule that then interacts with the canopy bow shock. By similar logic, the peak tension that is observed for the case with the Viking capsule is also lower. Interestingly, this case also observes the suspension lines undergoing compression following the peak tension. This, of course, should represent a state of slack in the suspension lines that physically do not withstand compressive loading, and in a future effort, a more representative constitutive relationship for the suspension lines/cable elements will be implemented. Despite these differences, the most interesting are the dynamics following peak tension. The case without the upstream Viking capsule is seen to undergo high frequency, low amplitude oscillations for the remainder of the sample period. The presence of the upstream Viking capsule, however, and the unsteady velocity profile that it provides to the parachute canopy, induce the large amplitude, low frequency 'breathing' cycles that are characteristic of DGB parachutes operating at Mach numbers above 1.5, implying that the breathing phenomenon can be attributed to the interaction of the canopy bow shock with the wake of a leading bluff capsule and is not inherent to DGB parachute designs in general.

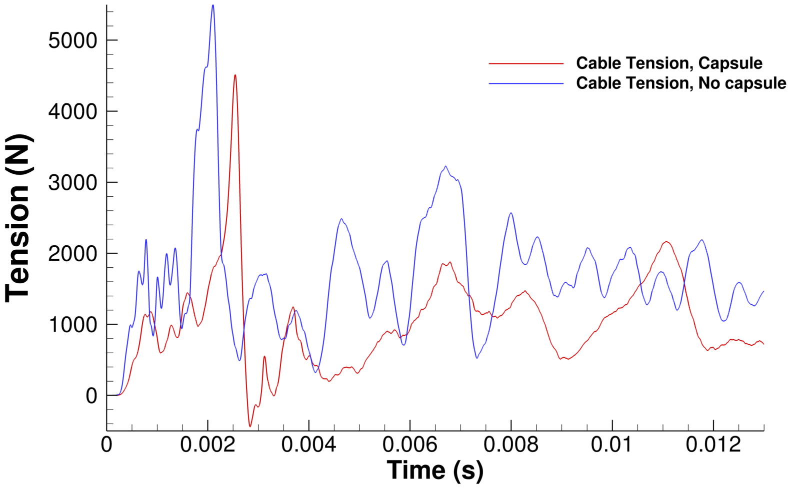

Figure 21: Time signal of the total tension in the 24 suspension lines for the cases considered here with and without the leading Viking capsule.

A closer look at the von Mises stress from a general simulation in the current work is presented in Figs. 22a-c at three snapshots in time during the inflation process. The von Mises stress distribution shows clear discontinuities along the thick broadcloth along the radials (which are thickened by a factor of 4 to represent the manufacturing of the canopy). These stress discontinuities along the radials have been the subject of some previous research studies,[53] and the ASPIRE missions observed shearing of the broadcloth material between the radials near the vent hole.[15] The structural resolution considered here is not fine enough to properly resolve the magnitude of the peak stresses, but it is clear from Figs. 19a-f that the stress starts to peak between the radial seams near the vent hole. This will be further investigated in future works with more representative structural constitutive relationships and sufficient mesh density to study potential paths to material failure and the different factors that contribute to this.

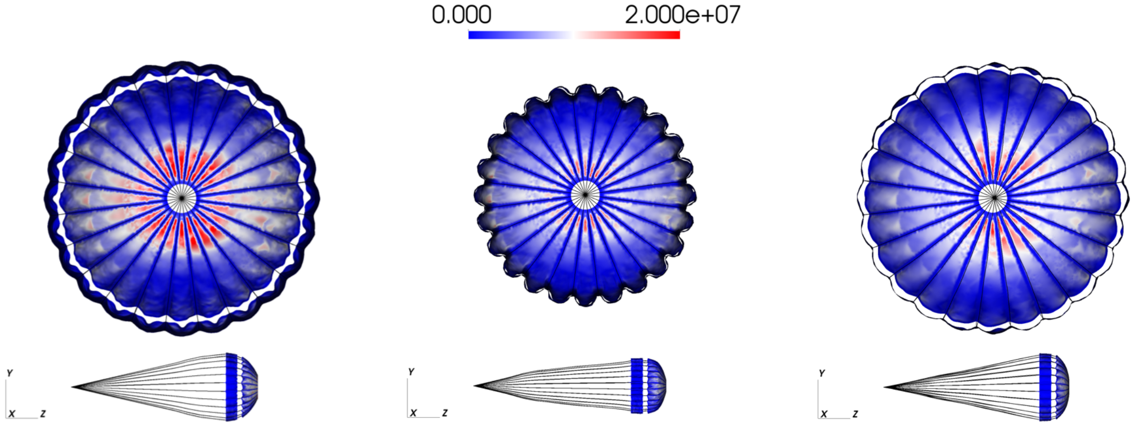

(a) (b) (c)

Figure 22: (a-c) Streamwise and spanwise views of saturated color contours of the von Mises stress distribution (Pa) on the CSD mesh at three instances in time from a general simulation in the current work. Notice the stress concentrations in the broadcloth material along the radials near the vent hole.

VI. Conclusion

This paper demonstrated extensions to our fluid-structure interaction method for simulating the inflation of parachutes in supersonic conditions. Specifically, a unique, parallel self-contact algorithm, a newly developed method for apply a porous media interface condition on a thin (below mesh resolution) geometry, improved sampling from the surrounding flow field, adaptive mesh refinement, and improved treatment of thin geometries in a immersed boundary solver framework were introduced and demonstrated individually and then on a sub-scale parachute geometry.

The next steps will be to apply these developments to realistic, full-scale parachute geometries, such as ASPIRE and MSL, and investigate the effect of the initial topology of the parachute on the quantities that were gathered during those tests, including coefficient of drag, total force coefficient, and suspension line tension.

VII. Acknowledgments

This work is partially supported by NASA ARMD's Transformational Tools and Technologies (T^3) project. Gokul Anugrah and Professor Brehm greatly acknowledge funding from the NASA Ames Computational Aerosciences Branch under contract 80NSSC18K0883. Computing resources are provided by NASA Advanced Supercomputing systems.

References

[1] Berndt, R. J., "Supersonic Parachute Research," Tech. rep., AERONAUTICAL SYSTEMS DIV WRIGHT-PATTERSON AFB OH FLIGHT ACCESSORIES LAB, 1962.

[2] Heinrich, H. G., "Aerodynamics of the supersonic guide surface parachute." *Journal of Aircraft*, Vol. 3, No. 2, 1966, pp. 105–111.

[3] Maynard, J. D., "Aerodynamic characteristics of parachutes at Mach numbers from 1.6 to 3," 1961.

[4] Steinberg, S., SIEMERS III, P. M., and Slayman, R. G., "velopment of the Viking Parachute Configuration by Wind-Tunnel Investigation," *Journal of Spacecraft and Rockets*, Vol. 11, No. 2, 1974, pp. 101–107.

[5] Murrow, H. N. and McFall Jr, J. C., "Some test results from the NASA planetary entry parachute program." *Journal of Spacecraft and Rockets*, Vol. 6, No. 5, 1969, pp. 621–623.

[6] Eckstrom, C. V. and Preisser, J. S., "Flight test of a 30-foot nominal diameter disk-gap-band parachute deployed at a Mach number of 1.56 and a dynamic pressure of 11.4 pounds per square foot," 1967.

[7] Way, D. W., Powell, R. W., Chen, A., and Steltzner, A. D., "Asymptotic parachute performance sensitivity," *2006 IEEE Aerospace Conference*, IEEE, 2006, pp. 9–pp.

[8] Sengupta, A., Wernet, M., Roeder, J., Kelsch, R., Witkowski, A., and Jones, T., "Supersonic testing of 0.8 m disk gap band parachutes in the wake of a 70 deg sphere cone entry vehicle," *20th AIAA Aerodynamic Decelerator Systems Technology Conference and Seminar*, 2009, p. 2974.

[9] Witkowski, A., Kandis, M., and Adams, D., "Inflation Characteristics of the MSL Disk Gap Band Parachute," *20th AIAA Aerodynamic Decelerator Systems Technology Conference and Seminar*, 2009, p. 2915.

[10] Witkowski, A., Kandis, M., Reuter, J., Machalick, W., Kelsch, R., and Sengupta, A., "Design of subscale parachute models for msl supersonic wind tunnel testing," *20th AIAA Aerodynamic Decelerator Systems Technology Conference and Seminar*, 2009, p. 2999.

[11] Barnhardt, M., Drayna, T., Nompelis, I., Candler, G., and Garrard, W., "Detached eddy simulations of the MSL parachute at supersonic conditions," *19th AIAA Aerodynamic Decelerator Systems Technology Conference and Seminar*, 2007, p. 2529.

[12] Karagiozis, K., Kamakoti, R., Cirak, F., and Pantano, C., "A computational study of supersonic disk-gap-band parachutes using Large-Eddy Simulation coupled to a structural membrane," *Journal of Fluids and Structures*, Vol. 27, No. 2, 2011, pp. 175–192.

[13] Gallon, J., Witkowski, A., Clark, I. G., Rivellini, T., and Adams, D. S., "Low density supersonic decelerator parachute decelerator system," *AIAA Aerodynamic Decelerator Systems (ADS) Conference*, 2013, p. 1329.

[14] Clark, I. G., Gallon, J. C., and Witkowski, A., "Parachute Decelerator System Performance During the Low Density Supersonic Decelerator Program's First Supersonic Flight Dynamics Test," *23rd AIAA Aerodynamic Decelerator Systems Technology Conference*, 2015, p. 2130.

[15] O'Farrell, C., Karlgaard, C., Tynis, J. A., and Clark, I. G., "Overview and reconstruction of the ASPIRE project's SR01 supersonic parachute test," *2018 IEEE Aerospace Conference*, IEEE, 2018, pp. 1–18.

[16] O'Farrell, C., Sonneveldt, B. S., Karhgaard, C., Tynis, J. A., and Clark, I. G., "Overview of the ASPIRE Project's Supersonic Flight Tests of a Strengthened DGB Parachute," *2019 IEEE Aerospace Conference*, IEEE, 2019, pp. 1–18.

[17] "Third ASPIRE Test Confirms Mars 2020 Parachute a Go," *NASA*, October 2018, pp. https://www.nasa.gov/feature/jpl/third–aspire–test–confirms–mars–2020–parachute–a–go.

[18] Lingard, J. and Darley, M., "Simulation of parachute fluid structure interaction in supersonic flow," *18th AIAA aerodynamic decelerator systems technology conference and seminar*, 2005, p. 1607.

[19] Lingard, J., Darley, M., and Underwood, J., "Simulation of Mars supersonic parachute performance and dynamics," *AIAA Paper*, Vol. 2507, 2007, pp. 2007.

[20] Yu, H., Pantano, C., and Cirak, F., "Large-Eddy Simulation of Flow Over Deformable Parachutes using Immersed Boundary and Adaptive Mesh," *AIAA Scitech 2019 Forum*, 2019, p. 0635.

[21] Huang, Z., Avery, P., Farhat, C., Rabinovitch, J., Derkevorkian, A., and Peterson, L. D., "Simulation of parachute inflation dynamics using an Eulerian computational framework for fluid-structure interfaces evolving in high-speed turbulent flows," *2018 AIAA Aerospace Sciences Meeting*, 2018, p. 1540.

[22] Borker, R., Huang, D., Grimberg, S., Farhat, C., Avery, P., and Rabinovitch, J., "Mesh Adaptation Framework for Embedded Boundary Methods for CFD and Fluid-Structure Interaction," *International Journal for Numerical Methods in Fluids*.

[23] Brehm, C., Barad, M. F., and Kiris, C. C., "An Immersed Boundary Method for Solving the Compressible Navier-Stokes Equations with Fluid-Structure Interaction," *54th AIAA Aviation and Aeronautics Forum, Washington, DC (Jun 13–17 2016)*, 2016.

[24] Boustani, J., Browne, O. M., Wenk, J. F., Barad, M., Kiris, C. C., and Brehm, C., "Fluid-Structure Interactions with Geometrically Nonlinear Deformations," *AIAA Science and Technology Forum and Exposition (AIAA SciTech 2019), San Diego, California (Jan 7–11 2019)*, 2019.

[25] C. Brehm, M.F. Barad, C. C. K., "Development of Immersed Boundary Computational Aeroacoustic Prediction Capabilities for Open-Rotor Noise," *JCP*, 2018.

[26] Brehm, C., Hader, C., and Fasel, H., "A Locally Stabilized Immersed Boundary Method for the Compressible Navier-Stokes Equations," *J. Comput. Phys.*, Vol. 295, 2015, pp. 475 – 504.

[27] Brehm, C. and Fasel, H., "A novel concept for the design of immersed interface methods," *J. Comput. Phys.*, Vol. 242, No. 0, 2013, pp. 234 – 267.

[28] Boustani, J., Barad, M. F., Kiris, C. C., and Brehm, C., "Fully-Coupled Fluid-Structure Interaction Simulations of a Supersonic Parachute," *AIAA Aviation Forum and Exposition (AIAA Aviation 2019), Dallas, Texas (June 17–21 2019)*, 2019.

[29] Brehm, C. and Fasel, H., "A novel concept for the design of immersed interface methods," *J. Comput. Phys.*, Vol. 242, No. 0, 2013, pp. 234 – 267.

[30] Brehm, C., Barad, M. F., and Kiris, C., "Development of immersed boundary computational aeroacoustic prediction capabilities for open-rotor noise," *Journal of computational physics*, 2018.

[31] Brehm, C., Barad, M. F., and Kiris, C. C., "Open Rotor Computational Aeroacoustic Analysis with an Immersed Boundary Method," *54th AIAA Aerospace Sciences Meeting*, 2016, AIAA-2016-0815.

[32] Kiris, C. C., Housman, J. A., Barad, M. F., Brehm, C., Sozer, E., and Moini-Yekta, S., "Computational framework for Launch, Ascent, and Vehicle Aerodynamics (LAVA)," *Aerospace Science and Technology*, Vol. 55, 2016, pp. 189–219.

[33] Brehm, C., Barad, M., Housman, J., and Kiris, C., "A comparison of higher-order finite-difference shock capturing schemes," *Computers & Fluids*, Vol. 122, 2015, pp. 184 – 208.

[34] Cescotto, S. and Charlier, R., "Frictional contact finite elements based on mixed variational principles," *International Journal for numerical methods in engineering*, Vol. 36, No. 10, 1993, pp. 1681–1701.

[35] Kucharski, S., Klimczak, T., Polijaniuk, A., and Kaczmarek, J., "Finite-elements model for the contact of rough surfaces," *Wear*, Vol. 177, No. 1, 1994, pp. 1–13.

[36] Laursen, T. A., "Formulation and treatment of frictional contact problems using finite elements." 1993.

[37] Schmidt, B. E., "Compressible Flow Through Porous Media with Application to Injection," Internal Report FM 2014.001, California Institute of Technology, 2015.

[38] Cruz, J. R., O'Farrell, C., Hennings, E., and Runnells, P., "Permeability of Two Parachute Fabrics-Measurements, Modeling, and Application," *24th AIAA Aerodynamic Decelerator Systems Technology Conference*, 2017, p. 3725.

[39] Browne, O. M. F., Haas, A. P., Fasel, H. F., and Brehm, C., "An efficient linear wavepacket tracking method for hypersonic boundary-layer stability prediction," *J. Comput. Phys.*, Vol. 380, 2019, pp. 243–268.

[40] Wagner, H., "Structures of thin sheet metal, their design and construction," 1928.

[41] Lu, K., Accorsi, M., and Leonard, J., "Finite element analysis of membrane wrinkling," *International Journal for numerical methods in engineering*, Vol. 50, No. 5, 2001, pp. 1017–1038.

[42] Pipkin, A. C., "Relaxed energy densities for large deformations of membranes," *IMA Journal of Applied Mathematics*, Vol. 52, No. 3, 1994, pp. 297–308.

[43] Mosler, J. and Cirak, F., "A variational formulation for finite deformation wrinkling analysis of inelastic membranes," *Computer Methods in Applied Mechanics and Engineering*, Vol. 198, No. 27-29, 2009, pp. 2087–2098.

[44] Lee, Y., Lee, P.-S., and Bathe, K.-J., "The MITC3+ shell element and its performance," *Computers & Structures*, Vol. 138, 2014, pp. 12–23.

[45] Zienkiewicz, O., Taylor, R., and Too, J., "Reduced integration technique in general analysis of plates and shells," *International Journal for Numerical Methods in Engineering*, Vol. 3, No. 2, 1971, pp. 275–290.

[46] Hughes, T. J., Cohen, M., and Haroun, M., "Reduced and selective integration techniques in the finite element analysis of plates," *Nuclear Engineering and design*, Vol. 46, No. 1, 1978, pp. 203–222.

[47] Spilker, R., "Invariant 8-node hybrid-stress elements for thin and moderately thick plates," *International Journal for Numerical Methods in Engineering*, Vol. 18, No. 8, 1982, pp. 1153–1178.

[48] Bathe, K.-J., *Finite element procedures*, Klaus-Jurgen Bathe, 2006.

[49] Lee, P.-S. and Bathe, K.-J., "Development of MITC isotropic triangular shell finite elements," *Computers & Structures*, Vol. 82, No. 11, 2004, pp. 945–962.

[50] Jeon, H.-M., Lee, Y., Lee, P.-S., and Bathe, K.-J., "The MITC3+ shell element in geometric nonlinear analysis," *Computers & Structures*, Vol. 146, 2015, pp. 91–104.

[51] Cen, S. and Shang, Y., "Developments of Mindlin-Reissner plate elements," *Mathematical Problems in Engineering*, Vol. 2015, 2015.

[52] Witkowski, A., Kandis, M., Sengupta, A., and Long, K., "Comparison of Subscale Versus Full-Scale Wind Tunnel Tests of MSL Disk Gap Band Parachutes," *20th AIAA aerodynamic decelerator systems technology conference and seminar*, 2009, p. 2914.

[53] Derkevorkian, A., Hill, J. L., Avery, P., Farhat, C., Rabinovitch, J., and Peterson, L. D., "Studies into Computational Modeling of Fabric in Inflatable Structures," *AIAA Scitech 2019 Forum*, 2019, p. 1028.